

## ABSTRACT

SOHAG, ZAHIRUL ISLAM. Synthesis and Photoelectrochemical Properties of Cu(I)-Containing Semiconducting Oxides. (Under the direction of Dr. Paul A. Maggard).

Metal-oxide compounds are promising materials for applications involving the conversion of solar energy into electrical power or chemical fuels. The motivation behind finding the new semiconducting oxides is driven by the ability of the sun to provide the energy required to drive the water splitting reaction to produce hydrogen and oxygen from water. Investigations of new *p*-type semiconductors as visible solar light photocatalysts are described herein. The copper(I)-containing metal oxides  $Cu_3Ta_7O_{19}$  and  $Cu_2Mo_{2.4}V_{1.6}O_{12}$  were synthesized via flux and solid-state synthetic methods, respectively. A synthetic route was found to yield  $Cu_3Ta_7O_{19}$  in high purity using a CuCl(10:1 molar ratio) flux at 800 °C (space group  $P6_3/m$  (no. 176),  $a = 6.2278(1)$  Å, and  $c = 20.1467(3)$  Å). The solid-state synthesis of  $Cu_2Mo_{2.4}V_{1.6}O_{12}$  was performed at 900 °C for 96h. The  $Cu_2Mo_{2.4}V_{1.6}O_{12}$  phase has a new structure type that was characterized using single crystal X-ray diffraction (space group  $C2$  (no. 5),  $a = 9.4830(3)$  Å,  $b = 3.69480(10)$  Å,  $c = 6.4696(2)$  Å and  $\beta = 111.4620(11)^\circ$ ). Members of the solid solution of  $Cu_3(Ta_{1-x}Nb_x)_7O_{19}$  ( $0 < x \leq 0.15$ ) were synthesized using flux synthesis methods. Substitution of Ta with Nb produces red shifts in the bandgap size from ~2.5eV to ~2.1eV for  $x = 0$  to  $x = 0.15$ . The photoelectrochemical properties were measured for *p*-type polycrystalline films of  $Cu_3(Ta_{1-x}Nb_x)_7O_{19}$  ( $0 < x \leq 0.15$ ) at pH~6.3 and exhibited strong cathodic photocurrents under visible-light irradiation. The results show that increasing the percentage of Nb in the structure, as well as heating the films to higher temperatures in air, both result in higher photocurrents. Heating the films in air at 250 °C for 20 minutes increases the photocurrents as well. Chronoamperometric measurements show that the polycrystalline

films exhibit a decay in their photocurrents that is a sensitive function of the film preparation conditions.

© Copyright 2015 by Zahirul Islam Sohag

All Rights Reserved

Synthesis and Photoelectrochemical Properties of Cu(I)-Containing Semiconducting Oxides

by  
Zahirul Sohag

A thesis submitted to the Graduate Faculty of  
North Carolina State University  
in partial fulfillment of the  
requirements for the degree of  
Master of Science

Chemistry

Raleigh, North Carolina

2015

APPROVED BY:

---

Paul A. Maggard  
Committee Chair

---

David A. Shultz

---

Elena Jakubikov

## **DEDICATION**

This work is dedicated to my parents Mizanur Rahman and Syeda Jahura Begum. Thank you for being there for me.

## **BIOGRAPHY**

Zahirul Sohag was born in Tangail, Bangladesh. In October 2012, he finished his undergraduate on Applied Chemistry & Chemical Engineering from the University of Dhaka. He has partook in an Internship from GlaxoSmithKline, Bangladesh in July 2012. He has worked in the environmental Chemistry and Materials Chemistry Lab of BCSIR(Bangladesh Council of Scientific and Industrial Research) in the end of 2011. In the fall of 2013 he joined North Carolina State University as a graduate student in Chemistry and after that he joined Maggard research group in October 2013 and started working on the synthesis and photoelectrochemical properties of Cu(I)-containing semiconducting metal-oxides .

## **ACKNOWLEDGMENTS**

I would like to thank my advisor, Dr. Paul Maggard for being a very supporting advisor for last couple of years. I really appreciate his guidance on my research work. Paul's passion for science has encouraged me a lot. Thanks to my committee members, Dr. David A. Shultz and Dr. Mike H. Whangbo for their feedback and suggestions.

I also want to thanks all the group members in Maggard research group, including Nacole, Lan, Ian, Jonathan and Brandon, for being so friendly and supportive. I really appreciate them for making the work environment enjoyable and fun. Their input and suggestion have helped me a lot with my graduate studies and research work. I want to thank Dr. Roger Sommer for taking the single crystal X-ray data and helping me with solving of the structure. I would also like to thank Chuck Mooney from Analytical Instrumentation Facility for the SEM images. Last but not least, thanks to my family and friends for their love and support.

## TABLE OF CONTENTS

<b>LIST OF TABLES</b> .....	vi
<b>LIST OF FIGURES</b> .....	vii
<b>PART 1. INTRODUCTION</b> .....	1
<b>CHAPTER 1. OVERVIEW</b> .....	2
<b>CHAPTER 2. EXPERIMENTAL TECHNIQUES</b> .....	9
<b>PART 2. RESULTS</b> .....	14
<b>CHAPTER 3. FLUX SYNTHESIS, CHARACTERIZATION, AND PHOTOELECTROCHEMISTRY OF <math>\text{Cu}_3\text{Ta}_7\text{O}_{19}</math> POLYCRYSTALLINE FILMS</b> .....	15
<b>CHAPTER 4. SOLID SOLUTIONS OF <math>\text{Cu}_3(\text{Ta}_{1-x}\text{Nb}_x)_7\text{O}_{19}</math> (<math>x \leq 0.15</math>): IMPACT OF Nb(V) SUBSTITUTION ON ITS STRUCTURE, BANDGAP SIZES AND PHOTOELECTROCHEMICAL PROPERTIES</b> .....	38
<b>CHAPTER 5. SOLID STATE SYNTHESIS AND CHARACTERIZATION OF <math>\text{Cu}_2\text{Mo}_{2.4}\text{V}_{1.6}\text{O}_{12}</math></b> .....	60
<b>CONCLUSION</b> .....	72
<b>REFERENCES</b> .....	75

## LIST OF TABLES

### CHAPTER 3

**Table 3-1.** Lattice constants, and volumes from cell refinement after 450°C oxidations ..... 35

**Table 3-2.** Lattice constants, and volumes from cell refinement after 550°C oxidations ..... 35

### CHAPTER 4

**Table 4-1.** Measured flat-band potentials vs SHE and calculated redox potential of the valence-band edge for  $\text{Cu}_3(\text{Ta}_{1-x}\text{Nb}_x)_7\text{O}_{19}$  films (pH ~6.3) ..... 49

**Table 4-2.** Thermogravimetric analysis of  $\text{Cu}_3(\text{Ta}_{1-x}\text{Nb}_x)_7\text{O}_{19}$  solid solutions at 450 °C for 20mins ..... 50

### CHAPTER 5

**Table 5-1.** Single crystal data for  $\text{Cu}_2\text{Mo}_{2.4}\text{V}_{1.6}\text{O}_{12}$  ..... 63

**Table 5-2.** Atomic coordinates and equivalent isotropic displacement parameters ( $\text{\AA}^2$ ) ..... 64

**Table 5-3.** Selected interatomic distances ( $\text{\AA}$ ) in the  $\text{Cu}_2\text{Mo}_{2.4}\text{V}_{1.6}\text{O}_{12}$  structure ..... 64

## LIST OF FIGURES

### CHAPTER 1

**Figure 1-1:** Solar Irradiation Spectrum as a function of photon wavelength while the visible-light wavelengths are indicated by the pink region ..... 3

**Figure 1-2:** Energy diagram of a photoelectrochemical cell with p-type semiconductor film (orange) on FTO glass (grey) as the working electrode which has a band gap size compatible to the visible-light energy spectrum..... 4

**Figure 1-3:** Relationship of the band positions and band gaps of several known metal-oxide semiconductors with the redox potentials for water splitting ..... 6

### CHAPTER 2

**Figure 2-1:** The Experimental Linear sweep voltammetry measurement setup ..... 11

### CHAPTER 3

**Figure 3-1.** Powder X-ray diffraction pattern of the calculated (a) and experimental data (b) for the flux-synthesized  $\text{Cu}_3\text{Ta}_7\text{O}_{19}$ . ..... 17

**Figure 3-2.** The Tauc plots of UV-Vis diffuse reflectance data for  $\text{Cu}_3\text{Ta}_7\text{O}_{19}$ , for its (a) direct bandgap (b) indirect bandgap sizes..... 19

**Figure 3-3.** Crystal structure of  $\text{Cu}_3\text{Ta}_7\text{O}_{19}$  illustrating (a) the overall unit cell, (b) coordination of the  $\text{TaO}_6$  octahedron and (c) edge sharing  $\text{TaO}_7$  pentagonal bipyramids..... 21

**Figure 3-4.** SEM images of  $\text{Cu}_3\text{Ta}_7\text{O}_{19}$  before heating (a,b), after heating to 350 °C for 60 min (c,d) ..... 22

**Figure 3-5.** SEM images of  $\text{Cu}_3\text{Ta}_7\text{O}_{19}$  after heating to 450 °C for 60 min (a,b), after heating to 550 °C for 60 min (c,d) 23

**Figure 3-6.** Current-potential curve in aqueous 0.5M  $\text{Na}_2\text{SO}_4$  solution at pH~6.3 under chopped visible light for  $\text{Cu}_3\text{Ta}_7\text{O}_{19}$  films annealed at 500 °C and no heating in air (red), or heated to 350 °C (blue), 450 °C (green), or 550 °C (magenta)..... 25

**Figure 3-7.** Chronoamperometry (−0.25V applied bias) in aqueous 0.5M  $\text{Na}_2\text{SO}_4$  solution at pH~6.3 under chopped visible light for  $\text{Cu}_3\text{Ta}_7\text{O}_{19}$  films annealed at 500 °C and no heating in air (black), or heated in air to 350 °C (red), 450 °C (green), or 550 °C (blue) for 20 minutes. .... 26

**Figure 3-8.** Current-potential curve in aqueous 0.5M  $\text{Na}_2\text{SO}_4$  solution at pH~6.3 under chopped visible light for  $\text{Cu}_3\text{Ta}_7\text{O}_{19}$  films annealed at 500 °C and heated in air to 350 °C for 20 minutes (red), 40 minutes (green), or 60 minutes (blue). .... 27

**Figure 3-9.** Chronoamperometry (−0.25V applied bias) in aqueous 0.5M  $\text{Na}_2\text{SO}_4$  solution at pH~6.3 under chopped visible light for  $\text{Cu}_3\text{Ta}_7\text{O}_{19}$  films annealed at 500 °C and heated in air at 350 °C for 20 minutes (black), 40 minutes (green), or 60 minutes (red)..... 28

**Figure 3-10.** Current-potential curve in aqueous 0.5M  $\text{Na}_2\text{SO}_4$  solution at pH~6.3 under chopped visible light for  $\text{Cu}_3\text{Ta}_7\text{O}_{19}$  films annealed at 500 °C and heated in air at 450 °C for 20 minutes (red), 40 minutes (green), or 60 minutes (blue). .... 29

**Figure 3-11.** Chronoamperometry (−0.25V applied bias) in aqueous 0.5M  $\text{Na}_2\text{SO}_4$  solution at pH~6.3 under chopped visible light for  $\text{Cu}_3\text{Ta}_7\text{O}_{19}$  films annealed at 500 °C and heated in air at 450 °C for 20 minutes (black), 40 minutes (red), or 60 minutes (green)..... 30

**Figure 3-12.** Current-potential curve in aqueous 0.5M Na<sub>2</sub>SO<sub>4</sub> solution at pH~6.3 under chopped visible light for Cu<sub>3</sub>Ta<sub>7</sub>O<sub>19</sub> films annealed at 500 °C and heated in air at 550 °C for 20 minutes (red), 40 minutes (green), or 60 minutes (blue). ..... 31

**Figure 3-13.** Chronoamperometry (-0.25V applied bias) in aqueous 0.5M Na<sub>2</sub>SO<sub>4</sub> solution at pH~6.3 under chopped visible light for Cu<sub>3</sub>Ta<sub>7</sub>O<sub>19</sub> films annealed at 500 °C and heated in air at 550 °C for 20 minutes (black), 40 minutes (red), or 60 minutes (green)...... 32

**Figure 3-14.** Powder XRD patterns of Cu<sub>3</sub>Ta<sub>7</sub>O<sub>19</sub> between 26° and 32° after heating to 350 °C for 20 minutes, 40 minutes, and 60 minutes ..... 33

**Figure 3-15.** Refined lattice parameters of Cu<sub>3</sub>Ta<sub>7</sub>O<sub>19</sub> after heating to 350 °C for 20 minutes, 40 minutes and 60 minutes. The upper graph (a) is a plot of the *a/b* lattice constants and the lower graph the unit cell volume (b), with error bars indicating estimated standard deviations. .... 34

**CHAPTER 4**

**Figure 4-1.** The indexed powder X-ray diffraction pattern of Cu<sub>3</sub>Ta<sub>7</sub>O<sub>19</sub>, including both experimental (top three) and calculated (bottom). ..... 39

**Figure 4-2.** Crystal structure of Cu<sub>3</sub>(Ta<sub>1-x</sub>Nb<sub>x</sub>)<sub>7</sub>O<sub>19</sub> illustrating (a) the overall unit cell, (b) edge sharing TaO<sub>7</sub>/ pentagonal bipyramids and (c) coordination of the TaO<sub>6</sub> octahedron. ....42

**Figure 4-3.** Refined *a/b* lattice parameters of Cu<sub>3</sub>(Ta<sub>1-x</sub>Nb<sub>x</sub>)<sub>7</sub>O<sub>19</sub> (0 < x ≤ 0.15) as a function of Nb content. .... 43

**Figure 4-4.** Refined *c* lattice parameter (a) and unit cell volume (b) of Cu<sub>3</sub>(Ta<sub>1-x</sub>Nb<sub>x</sub>)<sub>7</sub>O<sub>19</sub> (0 < x ≤ .15) as a function of Nb content. .... 44

**Figure 4-5.** Tauc plots of the direct (a) and indirect (b) band gap transitions of the  $\text{Cu}_3(\text{Ta}_{1-x}\text{Nb}_x)_7\text{O}_{19}$  ( $0 < x \leq 0.15$ ) solid solution compositions..... 46

**Figure 4-6.** SEM images of  $\text{Cu}_3(\text{Ta}_{1-x}\text{Nb}_x)_7\text{O}_{19}$  solid solutions with 0% Nb (a), 5% Nb (b), 10% Nb (c) and 15% Nb (d) content. .... 47

**Figure 4-7.** TGA analysis of  $\text{Cu}_3(\text{Ta}_{1-x}\text{Nb}_x)_7\text{O}_{19}$  films at 450 °C for 20 mins and ramping up and down time of 15 and 10 mins respectively..... 48

**Figure 4-8.** Mott-Schottky measurements of  $\text{Cu}_3(\text{Ta}_{1-x}\text{Nb}_x)_7\text{O}_{19}$  with the applied potential from 0.3 to -0.3V at pH ~6.3 ..... 50

**Figure 4-9.** Current-potential curves in aqueous 0.5M  $\text{Na}_2\text{SO}_4$  solution at pH~6.3 under chopped visible light for  $\text{Cu}_3(\text{Ta}_{1-x}\text{Nb}_x)_7\text{O}_{19}$  ( $x = 0, 0.02, 0.05$ ) films annealed at 500 °C and no heating in air ..... 52

**Figure 4-10.** Current-potential curves in aqueous 0.5M  $\text{Na}_2\text{SO}_4$  solution at pH~6.3 under chopped visible light for  $\text{Cu}_3(\text{Ta}_{1-x}\text{Nb}_x)_7\text{O}_{19}$  ( $x = 0.05, 0.1, 0.15$ ) films annealed at 500 °C and no heating in air ..... 53

**Figure 4-11.** Chronoamperometry (-0.25V applied bias) in aqueous 0.5M  $\text{Na}_2\text{SO}_4$  solution at pH~6.3 under chopped visible light for  $\text{Cu}_3(\text{Ta}_{1-x}\text{Nb}_x)_7\text{O}_{19}$  films annealed at 500 °C and no heating in air for 0% Nb (black), 2% Nb (red), 5% Nb (green), 10% Nb (blue), 15% Nb (cyan).)..... 54

**Figure 4-12.** Current-potential curve in aqueous 0.5M  $\text{Na}_2\text{SO}_4$  solution at pH~6.3 under chopped visible light for  $\text{Cu}_3(\text{Ta}_{1-x}\text{Nb}_x)_7\text{O}_{19}$  ( $x = 0.02$ ) films annealed at 500 °C and not heated

in air (black), or heated in air at 250 °C (red), 350 °C (green), or 450 °C (blue) for 20 minutes..... 55

**Figure 4-13.** Current-potential curve in aqueous 0.5M Na<sub>2</sub>SO<sub>4</sub> solution at pH~6.3 under chopped visible light for Cu<sub>3</sub>(Ta<sub>1-x</sub>Nb<sub>x</sub>)<sub>7</sub>O<sub>19</sub> (x = 0.05) films annealed at 500 °C and not heated in air (black), or heated in air at 250 °C (red), 350 °C (green), or 450 °C (blue) for 20 minutes ..... 56

## CHAPTER 5

**Figure 5-1.** Polyhedral views with the projections along *b*-axis (a) and *c*-axis (b) of the unit cell of Cu<sub>2</sub>Mo<sub>2.4</sub>V<sub>1.6</sub>O<sub>12</sub>..... 61  
and no oxidation.....53

**Figure 5-2.** Polyhedral view with the (a) Cu-layers along *c*-axis of Cu<sub>2</sub>Mo<sub>2.4</sub>V<sub>1.6</sub>O<sub>12</sub> and (b) Mo-layer along *c*-axis ..... 62

**Figure 5-3.** The indexed powder X-ray diffraction data for Cu<sub>2</sub>Mo<sub>2.4</sub>V<sub>1.6</sub>O<sub>12</sub> with the experimental (a) and calculated (b) patterns shown. The Miller indices (*h*, *k*, *l*) are shown on the calculated pattern ..... 65

**Figure 5-4.** Scanning-electron microscopy images of the surfaces of a Cu<sub>2</sub>Mo<sub>2.4</sub>V<sub>1.6</sub>O<sub>12</sub> particle (a and b) and energy dispersive X-ray spectroscopy of a Cu<sub>2</sub>Mo<sub>2.4</sub>V<sub>1.6</sub>O<sub>12</sub> particle (c and d)..... 66

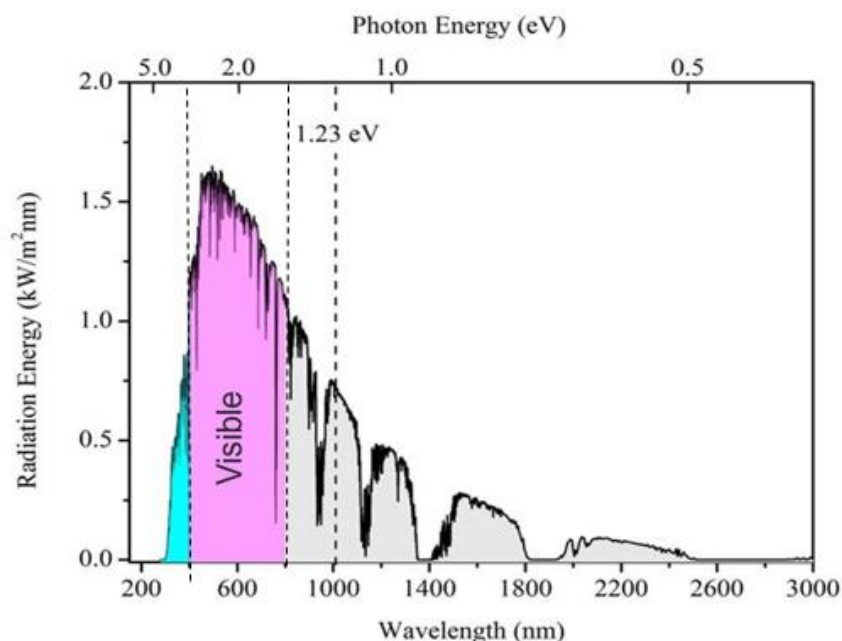
**Figure 5-5.** Tauc plots of direct (a) and indirect (b) bandgap of Cu<sub>2</sub>Mo<sub>2.4</sub>V<sub>1.6</sub>O<sub>12</sub> ..... 67

**PART 1**  
**INTRODUCTION**

## CHAPTER 1

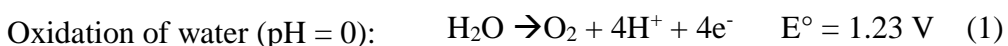
### OVERVIEW

In the last 40 years the world's primary energy consumption has been increasing at 2.2% per year as a result of population growth and increasing industrialization.<sup>1</sup> The current world population is at more than 7 billion people with a total energy consumption of 15TW. These numbers are estimated to grow to ~9 billion and 30TW respectively by 2050.<sup>2</sup> Presently, over 85% of energy use is fossil-fuel based, coming from natural gas, coal and oil. The unchecked growing need for fossil fuel energy is causing local pollution, global warming, and growing deficit between need and demand.<sup>3</sup> Burning of fossil fuels is one of the main sources of greenhouse gases like CO<sub>2</sub>, SO<sub>x</sub> and NO<sub>x</sub>.<sup>4</sup> To make sure that the world does not fall short of its energy needs, the near-unlimited supply potential of sustainable energy sources should be utilized. The utilization of abundant solar energy is an attractive method for helping to solve this energy crisis. One potential technological solution is to utilize heterogeneous photocatalytic semiconductors to convert sunlight into chemical fuels. A major portion of the solar spectrum is in the visible energy region (~92%). Thus, the absorption of visible-light energies and its use for the production of chemical or electrical energy represents an important and timely technological challenge. The first demonstration of the photocatalytic splitting of water and the production of hydrogen and oxygen was reported four decades ago by Fujishima and Honda.<sup>5</sup> In this case, *n*-doped TiO<sub>2</sub> semiconductor was used as the photocatalyst, which however, only works under UV irradiation. Thus, it is crucial to discover new semiconductor materials which can be used under sunlight more efficiently.



**Figure 1-1.** The solar irradiation spectrum as a function of photon wavelength with the visible-light wavelengths indicated by the pink region.<sup>6</sup>

In semiconductor materials the valence and conduction bands are separated by a forbidden region which is referred to as its band gap. If the energy of the incident light is larger than the band gap, electrons from the valence band are excited into the conduction band, and leaving behind a hole in the valence band. These excited electrons and holes may drive redox reactions. In water splitting mechanism the electrons reduce water to form  $H_2$  and holes can oxidize the water to form  $O_2$ . The band gap width and the energetic position of the valence and conduction band are very crucial in the selection of the appropriate photocatalyst for the water splitting.<sup>7</sup> An effective water splitting photocatalyst will have a valence band (VB) and conduction band (CB) energy that, respectively, are lower than the oxidation potential of water and higher than the reduction potential of protons. It also has to be stable against corrosion at its surfaces. A photoelectrochemical cell for water splitting involves the following reactions:



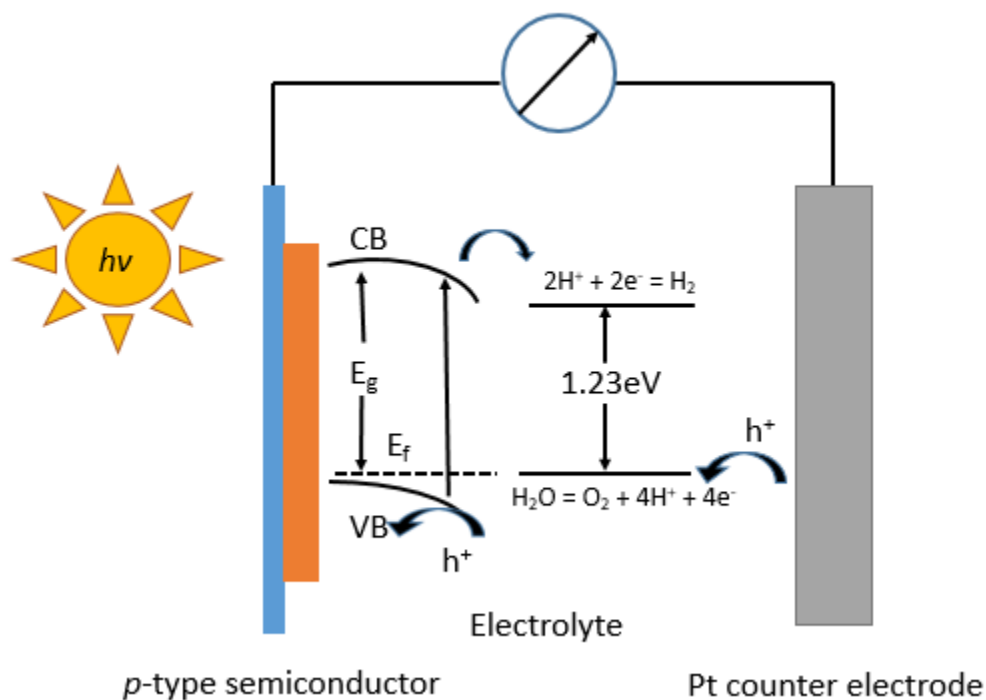
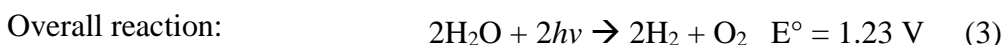
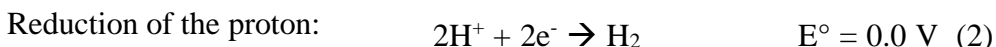


**Figure 1-2.** Energy diagram of a photoelectrochemical cell with *p*-type semiconductor film (orange) on FTO glass (grey) as the working electrode; this cell has a band gap size compatible with the visible-light energy spectrum.

The performance of the photoelectrodes in solar energy conversion require some specific properties that need to be considered such as the production of photocurrent, its stability, and the energy band positions.<sup>8</sup> Photocurrent-voltage measurements are an important measurement to resolve the performance characteristics of the photoelectrode. Other parameters, like the sign of the photocurrent, photocurrent density, electron vs. hole-transport limitations are also essential.<sup>3</sup> Current-voltage measurements, or linear-sweep voltammetry, is performed by chopping the irradiation on and off by a constant time interval, giving the

photocurrent (current flows under light irradiation) and dark current (current flows under no light irradiation) while sweeping the applied potential at a constant scan rate (1 and 50mV/s).<sup>9</sup> Chronoamperometric (current-time) measurements are another types of measurement used to determine the stability of the semiconductor photoelectrode over time at a constant applied potential. For a stable electrode, the observed photocurrent should be constant throughout the measurement.

For the generation of H<sub>2</sub> gas by photoelectrolysis of water, metal oxide semiconductors are some of the most promising materials.<sup>10</sup> Numerous metal-oxide semiconductor particles have been found to be photocatalytically active in aqueous suspensions such as, TiO<sub>2</sub>,<sup>11</sup> La<sub>2</sub>Ti<sub>2</sub>O<sub>7</sub>,<sup>12</sup> and Sr<sub>2</sub>Nb<sub>2</sub>O<sub>7</sub>.<sup>13</sup> Other metal-oxides which are also widely investigated as *p*-type or *n*-type photoelectrodes include ZnO,<sup>14,15</sup> BiVO<sub>4</sub>,<sup>16</sup> Cu<sub>2</sub>O,<sup>17,18</sup> and SrTiO<sub>3</sub>.<sup>19</sup> Metal-oxides TiO<sub>2</sub>, SrTiO<sub>3</sub> and ZnO do not absorb visible-solar light due to their wider band gap size. Solid solutions of In<sub>1-x</sub>Ni<sub>x</sub>TaO<sub>4</sub> (x = 0 to 0.2), have previously been used as photocatalysts under visible light with a 0.66% quantum yield.<sup>20</sup> For smaller band gap semiconductors, the band positions are also an important factor in determination of an effective photocatalyst. For example, WO<sub>3</sub> and Fe<sub>2</sub>O<sub>3</sub> are not suitable visible-light photocatalysts, even though they have lower band gap sizes, owing to their conduction band edges being less negative than the reduction potential of water.<sup>21,22</sup> Other important criteria include having a high mobility of charge carriers and efficient electron-hole separation.

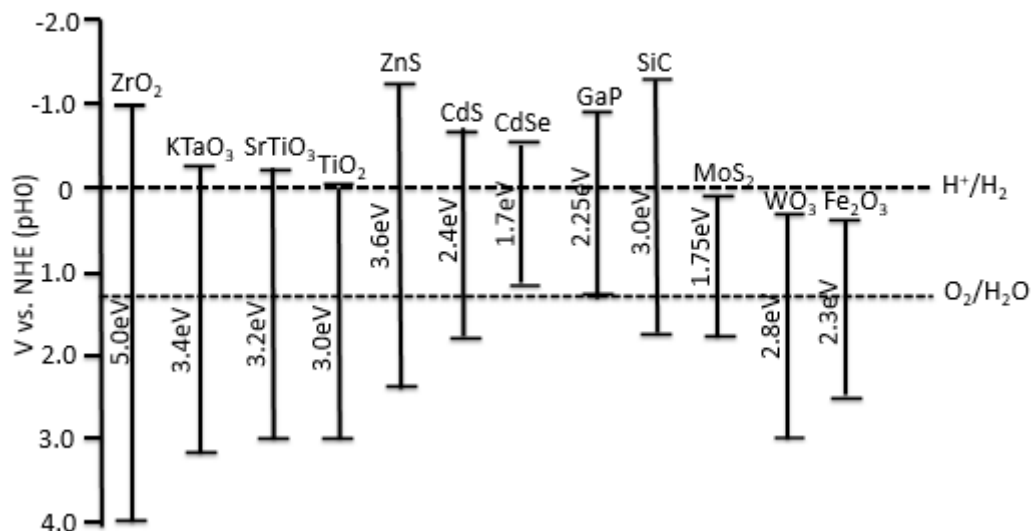
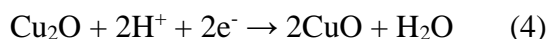


**Figure 1-3.** Relationship of the band positions and band gaps (pH = 0) of several known metal-oxide semiconductors with the redox potentials for water splitting.

Very few *p*-type semiconducting metal oxides have been studied for visible-light photocatalysis including,  $\text{Fe}_2\text{O}_3$ ,<sup>21,23</sup>  $\text{CaFe}_2\text{O}_4$ ,<sup>22,23</sup>  $\text{GaP}$ <sup>26</sup> and  $\text{Cu}_2\text{O}$ .<sup>17,18</sup> Although these materials have lower band gap sizes, relatively low photocurrents in aqueous solutions because of their weak hole mobility or instability against corrosion. For example, it has been shown that in solution under irradiation that *p*-type  $\text{Cu}_2\text{O}$  reduces to copper metal at the surfaces.<sup>27,28</sup> The decomposition of  $\text{Cu}_2\text{O}$  occurs due to the electrons produced by the excitation (equation 4).



The use of a co-catalyst on the surface or other modifications of the film surface can help to stabilize the film.<sup>29</sup> For example, the  $\text{Bi}_2\text{MNbO}_7$  ( $\text{M} = \text{Al}, \text{Ga}, \text{In}$  and  $\text{Y}$ , rare earth, and  $\text{Fe}$ ),  $\text{BiMO}_4$  ( $\text{M} = \text{Nb}^{5+}, \text{Ta}^{5+}$ ) and  $\text{InMO}_4$  ( $\text{M} = \text{Nb}^{5+}, \text{Ta}^{5+}$ ) compounds have been used as visible light photocatalysts with co-catalysts such as  $\text{Pt}$ ,  $\text{RuO}_2$  and  $\text{NiO}_x$  deposited onto their surfaces.<sup>30</sup>

By contrast, new mixed-metal oxides can be prepared with appropriate bandgap sizes for visible-light absorption by choosing a combination of transition metals that have filled and empty  $d$ -orbitals.<sup>31</sup> In these cases it is also possible to manipulate the valence and conduction band energies of the semiconductor. The relatively low energies of the oxygen  $2p$ -orbitals at the valence band edge is the primary reason behind the higher band gap sizes for the metal oxides. Transition and post transition-metals with  $d^{10}$  or  $d^{10}s^2$  electronic configuration can be incorporated into mixed-metal oxides, resulting in new higher energy valence that reduces the band gap size. This yields new valence band energies for enabling the water redox reaction under visible-light irradiation.<sup>11,32</sup> There are several possible candidates for the mixed-metal oxides that combine  $d^0$  metal cations (e.g.,  $Ta^{5+}$ ,  $Nb^{5+}$ ,  $W^{6+}$ ,  $Mo^{6+}$ ,  $V^{5+}$  and  $Zr^{4+}$ ) with  $d^{10}$  or  $d^{10}s^2$  metal cations ( e.g.,  $Ag^+$ ,  $Zn^{2+}$ ,  $Cu^+$ ,  $Bi^{3+}$ ,  $Pb^{2+}$ ).

Several mixed-metal oxide systems containing Cu(I) combined with Ta(V), Nb(V) and V(V) have been investigated by the Maggard research group. These systems are advantageous over other metal oxides owing to their lower band gap sizes ( $\sim 1.3$ - $2.6$  eV) and high photocurrent densities ( $\sim 1$ - $3$  mA/cm<sup>2</sup>) as photocathodic polycrystalline films. All of the known phases of Cu(I) niobates have relatively small band gap sizes, e. g.,  $CuNb_3O_8$  ( $\sim 1.4$  eV),<sup>34</sup>  $Cu_2Nb_8O_{21}$  ( $\sim 1.6$  eV)<sup>34</sup> and  $CuNbO_3$  ( $\sim 2.0$  eV)<sup>35</sup> and exhibit strong photocurrents under visible-light when deposited onto FTO slides as polycrystalline films. In the Cu(I) tantalate system, the  $Cu_2Ta_4O_{11}$ ,  $Cu_3Ta_7O_{19}$ , and  $Cu_5Ta_{11}O_{30}$  compounds have lower band gap sizes ( $\sim 2.3$ - $2.6$  eV) and promising photoelectrochemical properties under visible-light.<sup>36,37</sup> Further, research efforts on solid solutions of  $Li_{1-x}Cu_xNb_3O_8$  and  $NaCu(Ta_{1-x}Nb_x)_4O_{11}$  have established the relationship between the band gap size and Cu(I) and Nb(V) content in the solid solutions. Their band gap sizes can be manipulated by tuning the composition of these solid solutions. For example, significant red shifting of the band gap was observed ( $\sim 3.89$  -  $1.45$  eV) in the case of  $Li_{1-x}Cu_xNb_3O_8$  (from  $x = 0$  to  $1$ ) as more Li(I) cations were replaced by Cu(I) cations, owing to the fact that Cu(I) cations raise the valence band edge energies.<sup>36</sup> For the  $NaCu(Ta_{1-x}Nb_x)_4O_{11}$  (from  $x = 0$  to  $0.7$ ) solid solution the conduction band was lowered in energy as more Ta(V) cations were replaced by Nb(V) cations, and thus the band gap size was reduced from

~2.65 eV to ~1.80 eV.<sup>37</sup> Thus, the tunability of the band gap sizes of the metal-oxide solid solutions need to be investigated which have a more optimal match with the water redox couples and visible light energy.

Presented here is the flux synthesis and photoelectrochemical properties of  $\text{Cu}_3\text{Ta}_7\text{O}_{19}$ , its solid solution  $\text{Cu}_3(\text{Ta}_{1-x}\text{Nb}_x)_7\text{O}_{19}$ , (from  $x = 0$  to 0.15), and the solid state synthesis of a new copper-molybdate/vanadate compound. A more detailed photoelectrochemical investigation of  $\text{Cu}_3\text{Ta}_7\text{O}_{19}$  was conducted than reported previously. The solid solution of  $\text{Cu}_3(\text{Ta}_{1-x}\text{Nb}_x)_7\text{O}_{19}$  was investigated to understand the effect of the chemical composition on its band gap sizes, photocurrent densities, and stabilities of the polycrystalline films under visible-light irradiation. Finally, the crystal structure of the new  $\text{Cu}_2\text{Mo}_{2.4}\text{V}_{1.6}\text{O}_{12}$  compound was solved by single crystal X-ray diffraction, and new measurements were taken of its bandgap size and photoelectrochemical properties.

## CHAPTER 2

### EXPERIMENTAL TECHNIQUES

**Flux Synthesis.** Flux synthesis reactions were carried out under nitrogen or argon in a glovebox. Analytical grade reactants were combined together in stoichiometric ratios and were well ground in a mortar and pestle for about 30 minutes with the addition of the desired flux. The reaction mixtures were loaded into fused silica tubes and flame sealed under vacuum. The reaction tubes were heated in a box furnace for the required reaction time with a ramping time of 4 hours. After each reaction the products were washed with 3M NH<sub>4</sub>OH multiple times in order to remove the flux and any excess reactants. Finally the products were typically dried in an oven at ~80°C.

**Powder X-ray Diffraction.** The products were characterized by high resolution Powder X-ray Diffraction (PXRD). PXRD data were collected on an Inel X-ray diffractometer using CuK<sub>α1</sub> radiation (1.54056 Å) from a sealed tube x-ray generator (30 mA, 35 kV) using a curved position sensitive detector (CPS 120) in transmission mode. Samples were prepared by depositing approximately 50 mg of each sample onto a piece of Scotch tape adhered to the sample holder. The sample was spread across the tape as a uniform smooth layer and a second piece of tape was then placed over that to hold the sample. Next, the sample holder was placed on a rotating mount located between the direct beam of the incident X-rays and the detector. Data were collected for approximately from 30-120 minutes. For the Cu-Mo-V system, high-resolution powder PXRD data were collected on a RIGAKU R-Axis Spider diffractometer (graphite monochromatized Cu K $\alpha$  radiation,  $\lambda=1.5406$ ) at room temperature. All PXRD data were analyzed using the Winplotr program,<sup>38</sup> and analyzed with reference to theoretical calculated patterns contained in the Inorganic Crystal Structure Database (ICSD) and the Powder Diffraction File (PDF) from FindIt.<sup>39</sup> The Rietveld method using whole pattern fitting (WPF) were used for the lattice refinements in the software program Jade.<sup>40</sup>

**UV-Visible Diffuse Reflectance Spectra.** UV-Visible Diffuse Reflectance Spectra (DRS) were collected on a Shimadzu UV-3600 using a BaSO<sub>4</sub> background. Approximately

50 mg of sample was mounted to a BaSO<sub>4</sub> pressed plate and placed along the external window. Pressed BaSO<sub>4</sub> plates were used as a reference and the data were plotted as the remission function as  $F(R_\infty) = (1 - R_\infty)^2 / (2R_\infty)$ , based on the Kubelka-Munk theory of diffuse reflectance which relates reflectance, R, to an absorption coefficient  $\alpha$  and a scattering coefficient,  $s$ .<sup>41</sup> Assuming a constant scattering coefficient  $s$ , F(R) will be proportional to  $\alpha$  and thus represents the absorbance of the sample. The wavelength is converted to photon energy by using the well-known formula  $eV = 1240 / \lambda$ , and the band gap of the metal oxide is estimated from the linear rise in the absorbance.

**Film Preparation.** TEK-15 fluorine-doped tin oxide (FTO) slides were used as the substrate in order to prepare the films. First, the FTO slides were sonicated in deionized water, ethanol and acetone respectively for 30 minutes each and dried in air at room temperature. Using Scotch 3M tape, a 1cm<sup>2</sup> area was taped off on the conducting side and the polycrystalline material was deposited using the drop casting and doctor blade method. As the dispersant for the powders, a water/tert-butanol solution was used. The sample was allowed to dry before removing the tape. The films were then annealed at 500 °C for 3 hours under dynamic vacuum. After annealing, the films were either used as is for PEC measurements or were heated in air for different times and temperatures.

**Photoelectrochemical Measurements.** The experimental setup consisted of a Teflon cell using a three electrode system, with the polycrystalline film as the working electrode, Pt as the counter electrode, and a standard calomel reference electrode (sat. KCl). Nitrogen gas was purged through the electrolyte solution (0.5 M Na<sub>2</sub>SO<sub>4</sub>, pH~ 6.3) for 30 min prior to, and during the experiments. The pH of the electrolyte solution was controlled with either 3M NaOH or 0.5M H<sub>2</sub>SO<sub>4</sub>. Electrochemical data were measured with a Princeton Applied Research, PARSTAT 2263 and accompanying PowerSuite software. Electrochemical data were obtained on a CH-Instruments 620A electrochemical analyzer.<sup>42</sup> Before putting the film into the cell, an outline of Scotch tape was applied to the sample area to remove any possible effect of the FTO glass at the electrolyte interface. A high-pressure Xenon lamp with IR and AM 1.5 G filters was used as a light source with a power density of ~100 mW/cm<sup>2</sup>. Linear

sweep voltammetry (LSV) measurements were performed using an applied bias range of 0.200 V to -0.600 V vs. SCE at a scan rate of 0.025 V/s. To investigate both dark current and photocurrent the light source was chopped during the measurements. Time-dependent photocurrents were measured at an applied bias -0.25V to observe the stability of the working electrode.

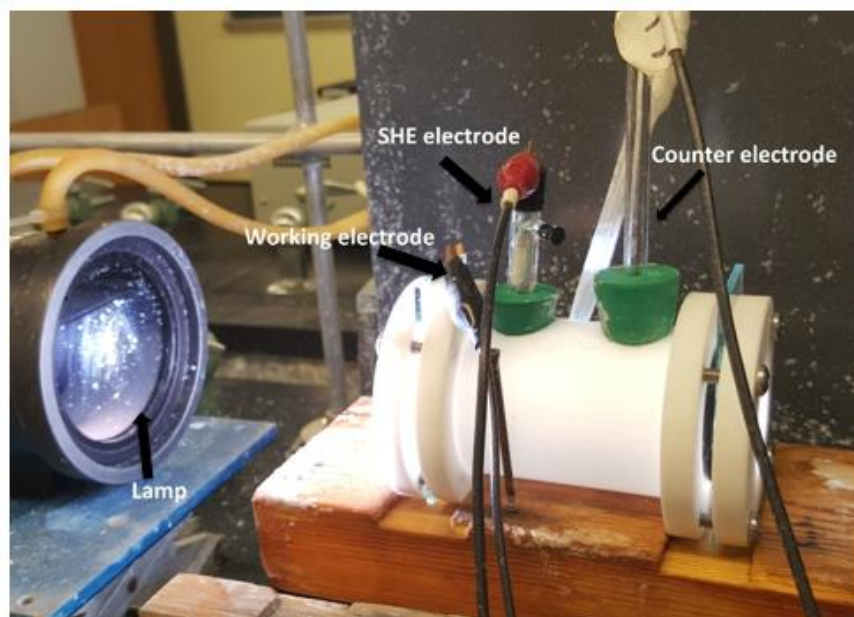


**Figure 2-1.** The experimental setup for photoelectrochemical measurements.

**Mott-Schottky Measurements.** Mott-Schottky measurements were performed in the dark. For each sample, a potential range of 0.3 to -0.3 V was applied within a frequency range of 25 KHz to 1 KHz. Mott-Schottky is an electrical impedance measurement which measures the capacitance of the semiconductor depletion region when the film is immersed in an aqueous solution.<sup>43</sup>

To relate the flat-band potential to the capacitance of a semiconductor, the Mott-Schottky equation is used. It is derived through a combination of Poisson's equation, the Boltzmann distribution, and Gauss' law.<sup>61</sup>

$$\frac{1}{C^2} = \left( \frac{2}{e\epsilon\epsilon_0 N_A A^2} \right) \left( -V_o + V_{fb} - \frac{kT}{e} \right) \quad (5)$$

In equation (5), the inverse capacitance squared ( $\frac{1}{C^2}$ ) of the space charge region at the semiconductor/electrolyte interface is calculated using the dielectric constant of the material ( $\epsilon$ ), vacuum permittivity ( $\epsilon_0, 8.85 \times 10^{-14} \text{ F/cm}$ ), donor density ( $N_D$ ), electron charge ( $e, 1.502 \times 10^{-19} \text{ C}$ ), applied bias ( $V$ ), flat-band potential ( $V_{fb}$ ), Boltzmann constant ( $k, 8.617 \times 10^{-5} \text{ eV/K}$ ), and temperature ( $T$ ). The acceptor density  $N_A$  is used in place of the donor density for  $p$ -type semiconductor, and the relevant signs in the equation are reversed. The measurement produces a linear plot when the frequency of the AC current is high enough that the capacitor element has a smaller resistance than the charge transfer resistance at the semiconductor/electrolyte interface. A linear plot is used to calculate the flat band potential by finding where the inverse capacitance squared extrapolates to zero. The flat-band can then be calculated from Equation (6).

$$V_{fb} = V_o + \frac{kT}{e} \quad (6)$$

The difference in the Fermi level of the semiconductor and redox position of the electrolyte before charge equilibrium is reached is indicated by the flat-band energy. After determination of the flat-band condition, the energy position of the valence band ( $E_v$ ) is calculated from Equation (7)

$$E_v = V_{fb} + kT \ln\left(\frac{N_A}{N_V}\right) \quad (7)$$

The term ( $N_A$ ) represents the density-of-states within the valence band, and is typically approximated as  $\sim 10^{19}$ .

**Single crystal X-ray Diffraction.** Single crystal X-ray data sets were collected on a Bruker SMART APEX-II CCD diffractometer using graphite-monochromatized Mo K $\alpha$  radiation ( $\lambda=0.71073$ ) from a sealed tube at 299 K. The initial unit cell determination and data reduction were carried out by the Bruker SAINT program.<sup>44</sup> Direct methods in SHELXS-97 were used to solve the structure.<sup>45</sup> Full matrix least-squares in SHELXS-97 was used in the final structure refinements.

**Thermogravimetric Analysis (TGA).** Weighted amounts of each sample were loaded onto a platinum pan on the TA instrument TGA Q50 analyzer. Equilibration of the pan was carried out at room temperature. Then the sample was heated to 450 °C at a rate of 15 °C / min under nitrogen flow (40 mL/min). The data are plotted as the percentage of starting weight versus time (min).

**Scanning Electron Microscopy (SEM).** A JOEL JSM-6400F field-emission scanning electron microscopy (FESEM) was used to record images of the samples. Double-sided carbon tape was used to hold  $\sim 10$ mg of the powder on the aluminum sample holder. A stream of nitrogen gas was applied to the sample on the tape to remove excess powder and ensure a distribution of sizes and morphologies on the carbon tape.

**PART 2**  
**RESULTS**

## CHAPTER 3

### THE FLUX SYNTHESIS, CHARACTERIZATION, AND PHOTOELECTROCHEMISTRY OF $\text{Cu}_3\text{Ta}_7\text{O}_{19}$ POLYCRYSTALLINE FILMS

#### Introduction

To face the growing demand for energy, utilization of solar energy is one of the best possible options.<sup>1</sup> As most of the incident Sunlight on the earth falls in visible range, the development of photoelectrodes that absorb visible light is a primary goal. Recently, Cu(I)-containing semiconductors have established a significant and rapidly growing research direction in this area. Most of the metal-oxides exhibit absorption in the higher ultraviolet energies of the solar spectrum (i.e.,  $E_g > 3.0$  eV) owing to their relatively large bandgap sizes. On the other hand, most Cu(I)-containing oxides contain higher-energy valence bands composed of the Cu  $3d^{10}$  orbitals, yielding light absorption deep into the visible region. Again, Cu(I)-containing oxides also show more negative potentials for their conduction band energies and are generally *p*-type semiconductors, making them suitable candidates for water splitting. Only a few *p*-type semiconducting oxides have been investigated such as  $\text{Cu}_2\text{O}$ ,<sup>17,18</sup>  $\text{CaFe}_2\text{O}_4$ ,<sup>24,25</sup> and metal ion-doped  $\text{Fe}_2\text{O}_3$ <sup>21,23</sup> that work as photocathodes under visible light condition.  $\text{Cu}_2\text{O}$  has shown high photocurrents and activities as a visible photocatalyst, but its instability makes it unsuitable.

Investigation of *p*-type semiconductors that consist of early and late transition metals is one research focus in the Maggard group. In this research approach, the reduction of bandgap sizes is achieved by combining transition metals with empty  $d^0$  orbitals (Nb (V)/ Ta (V)) in the conduction band and  $d^{10}$  orbitals (Cu (I) cation) in the valence band.<sup>46,37</sup> Heating of the *p*-type Cu(I)-niobate and Cu(I)-tantarate polycrystalline films in air from 350 to 550 °C yields the highest cathodic photocurrents. Recently  $\text{CuNb}_3\text{O}_8$ ,  $\text{Cu}_2\text{Nb}_8\text{O}_{21}$  and  $\text{Cu}_5\text{Ta}_{11}\text{O}_{30}$  phases were found to show Cu vacancies and the formation of CuO nanoislands on the surfaces under these heating conditions. Higher photocurrents are observed for the films after heating in air. Another Cu(I)-tantarate,  $\text{Cu}_3\text{Ta}_7\text{O}_{19}$ , has a band gap size (i.e., ~2.5 eV) and conduction band potential

(i.e., -1.57 V vs RHE) which satisfies the thermodynamic condition for the water reduction under visible-light irradiation.

The light-stimulated reduction of water by  $\text{Cu}_3\text{Ta}_7\text{O}_{19}$  represents a potentially promising route for the production of hydrogen gas owing to the fact that it has a visible-light bandgap size ( $\sim 2.5$  eV). It is also a *p*-type semiconductor with a high energy conduction band.<sup>37</sup> Presented herein is the CuCl-mediated flux synthesis and in-depth photoelectrochemical investigation of  $\text{Cu}_3\text{Ta}_7\text{O}_{19}$  polycrystalline films that function as photocathodes under visible light irradiation.

## **Experimental Section**

### **Materials**

The reagents were used as purchased without any further modification. The reactants were reagent grade  $\text{Ta}_2\text{O}_5$  (Alfa Aesar, min 99.99%),  $\text{Cu}_2\text{O}$  (Alfa Aesar, 99.99%), and CuCl (Alfa Aesar, 99.99%) as the flux medium. For the photoelectrochemical measurements,  $\text{Na}_2\text{SO}_4$  (Alfa Aesar, 99.0%), NaOH (>97%, Fisher Scientific), and deionized water were used.

### **Synthesis**

A molten-salt flux reaction was used in the synthesis of  $\text{Cu}_3\text{Ta}_7\text{O}_{19}$  with CuCl as the flux. Stoichiometric amounts of  $\text{Cu}_2\text{O}$  (Alfa Aesar 99.99%) and  $\text{Ta}_2\text{O}_5$  (Alfa Aesar 99.99%) were mixed and combined with CuCl (Alfa Aesar 99.9%) in a 10:1 molar ratio (flux/product). These were ground together in a mortar and pestle for around 30 minutes to give a homogenous powder in an argon atmosphere in a glovebox. The reactant mixture was loaded into a cleaned quartz tube and flame sealed on a vacuum line. This was then heated to 800 °C for 26 hours. After cooling, the resulting products were washed with 3M  $\text{NH}_4\text{OH}$  in order to remove the CuCl flux and excess  $\text{Cu}_2\text{O}$ , yielding a bright yellow powder. All products were characterized with powder X-ray diffraction and UV-Vis spectroscopic methods. The product was pure according to powder XRD.

## Characterization

### X-ray Diffraction Techniques

An Inel X-ray diffractometer using Cu K $\alpha$ 1 radiation ( $\lambda = 1.54056 \text{ \AA}$ ) from a sealed tube X-ray generator (30 mA, 35 kV) was used to take powder XRD data. To obtain diffractograms a curved position sensitive detector (CPS-120) was used in transmission mode. Two pieces of Scotch tape was used with a sample mass of  $\sim 50 \text{ mg}$  and rotated between the X-ray beam and detector. Data collection times were from 30 to 90 min. All of the data were plotted using the WinPlotr software program.

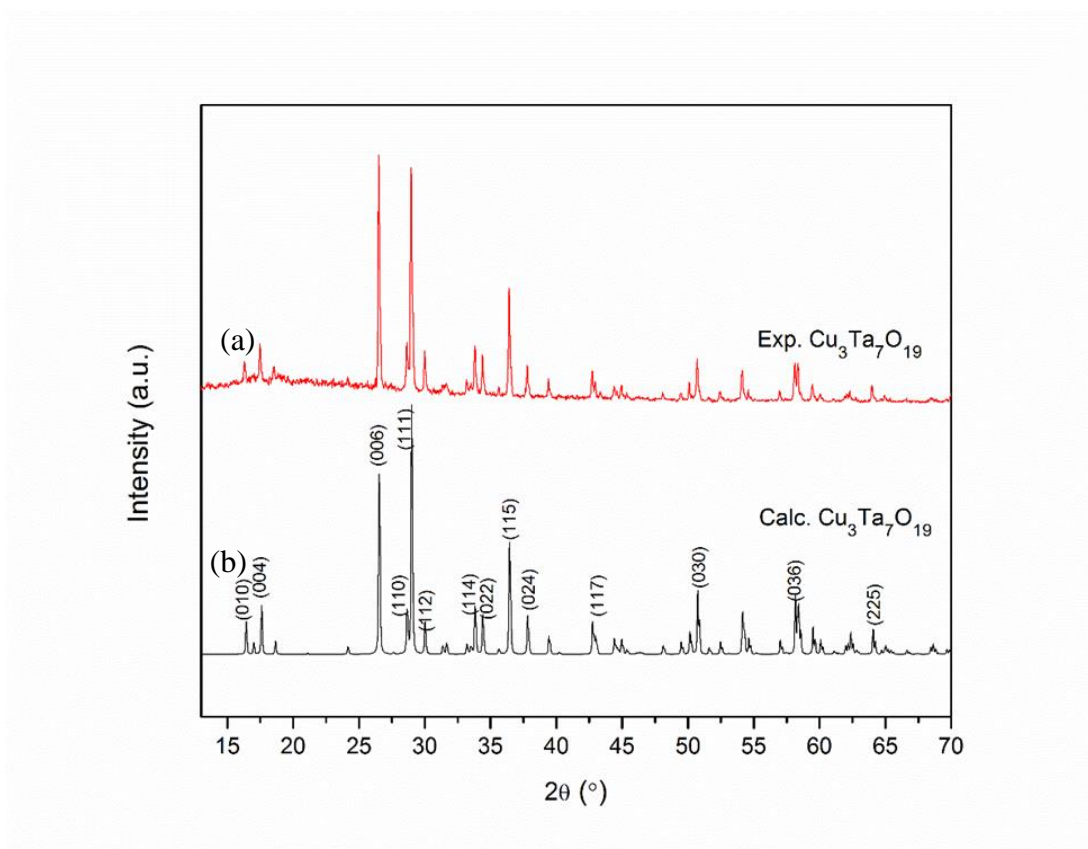


**Figure 3-1.** Powder X-ray diffraction pattern of the calculated (a) and experimental data (b) for the flux-synthesized  $\text{Cu}_3\text{Ta}_7\text{O}_{19}$ .

## Optical Characterization

A Shimadzu spectrophotometer UV-3600 was used to collect UV-Vis diffuse reflectance data using an integrating sphere within the wavelength range of 200 nm to 1300 nm. Around 30 mg of powder sample was mounted onto a sample holder by pressing the sample into a BaSO<sub>4</sub> matrix. Then it was placed on the external window of the integrating sphere. The reflectance data were plotted as  $F(R_{\infty})$  versus energy (eV), where  $F(R_{\infty}) = ((1 - R_{\infty})^2 / (2R_{\infty})) = \alpha/s$  according to the Kubelka–Munk theory of diffuse reflectance which relates reflectance,  $R$ , to the absorption coefficient,  $\alpha$ , and the scattering coefficient,  $s$ . The Tauc equation was used to calculate both the direct and indirect bandgap energies of the metal-oxide semiconductor, where  $\alpha$  is the absorption coefficient,  $h\nu$  is the energy in eV, and  $E_g$  is the bandgap.

$$(\alpha h\nu)^n = (h\nu - E_g)$$

. The bandgap energies of the direct and indirect excitations of a semiconductor can be extracted from linear extrapolations of  $\{[F(R)h\nu]^2 \text{ vs. } h\nu\}$  and  $\{[F(R)h\nu]^{1/2} \text{ vs. } h\nu\}$ , respectively, as plotted in Figure 3-2. The indirect and direct bandgaps were found to be ~2.3 eV and ~2.5 eV, respectively.

Scanning electron microscopy (SEM) images were taken on a JEOL JSM-6400F field-emission scanning electron microscope to characterize particle morphologies, surfaces features, and chemical compositions of Cu<sub>3</sub>Ta<sub>7</sub>O<sub>19</sub> particle.

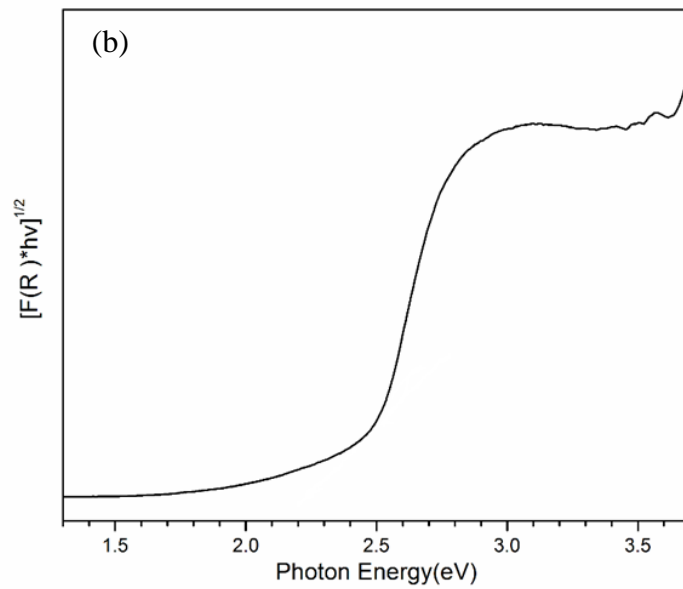
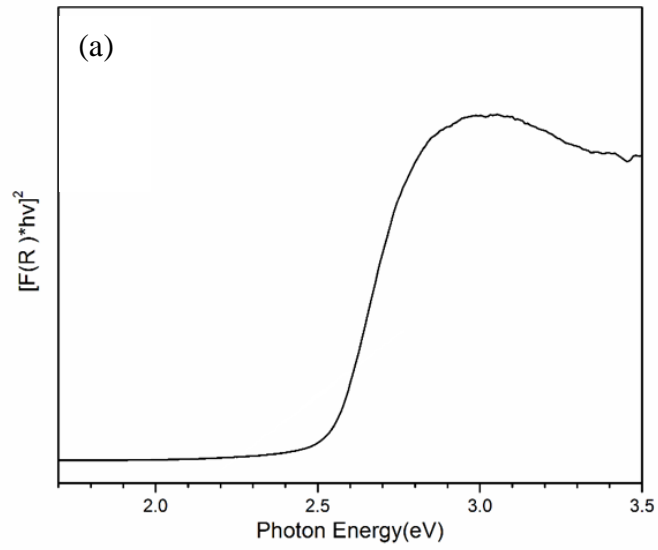


**Figure 3-2.** The Tauc plots of UV-Vis diffuse reflectance data for  $\text{Cu}_3\text{Ta}_7\text{O}_{19}$ , for its (a) direct bandgap (b) indirect bandgap sizes.

## Film Preparation and Photoelectrochemical Measurements.

All polycrystalline films were prepared on TEK-15 fluorine-doped tin oxide (FTO) slides. The FTO slides were sonicated in deionized water, ethanol and acetone respectively for 30 minutes each and dried in air at room temperature. Using Scotch 3M tape, a 1cm<sup>2</sup> area was taped off on the conducting side and the polycrystalline material was deposited using the drop casting and doctor blade method. As the dispersant for the powders, a water/tert-butanol solution was used. The sample was allowed to dry before removing the tape. The films were then annealed at 500°C for 3 hours under dynamic vacuum. After annealing, the films were either used as is for PEC measurements or heated in air for different times and temperatures. Polycrystalline films of Cu<sub>3</sub>Ta<sub>7</sub>O<sub>19</sub> were examined in a photoelectrochemical cell for measurement of the current density and photostability using 0.5M Na<sub>2</sub>SO<sub>4</sub> solution as electrolyte and at pH of ~6.3. The films were heated in air at 350 °C, 450 °C and 550 °C for 20 minutes. Linear-sweep cyclic voltammetric measurements of polycrystalline films were performed with applied potentials of 0.2V to -0.6. Chronoamperometric measurements were also carried out for the polycrystalline films to their stability. During these measurements, a constant bias (-0.25V) was applied for 1,000 seconds and the current density was measured as a function of time. A high pressure xenon lamp (Newport Corporation) was used as the light source. The lamp was fitted with infrared and ultraviolet light cutoff filters (1000 nm > λ > 420 nm). The irradiant power density was measured to be ~500 mW/cm<sup>2</sup>.

## Results and Discussion

### Structure

As previously reported, Cu<sub>3</sub>Ta<sub>7</sub>O<sub>19</sub> crystallizes in the hexagonal P6<sub>3</sub>/m space group. Its crystalline structure has been described previously ( $a = 6.2278(1) \text{ \AA}$ ,  $b = 6.2278(1) \text{ \AA}$ ,  $c = 20.1467(3) \text{ \AA}$ , and  $\beta = 120^\circ$ ).<sup>42</sup> Figure 3-3(a) shows an overall view of the unit cell along the [110] direction. The structure is comprised of linearly coordinated Cu(I) cations and edge-sharing pentagonal bipyramidal TaO<sub>7</sub> double layers. Figure 3-3(b) shows the local

coordination of TaO<sub>7</sub> layer that also serves to form the TaO<sub>6</sub> octahedron with the axial oxygen atoms. Six linearly coordinated Cu(I) cation surround each TaO<sub>6</sub> octahedron. Figure 3-3(c) represents the structural views down [0 0 1] of Cu<sub>3</sub>Ta<sub>7</sub>O<sub>19</sub> that clarifies the edge-sharing TaO<sub>7</sub> layer.

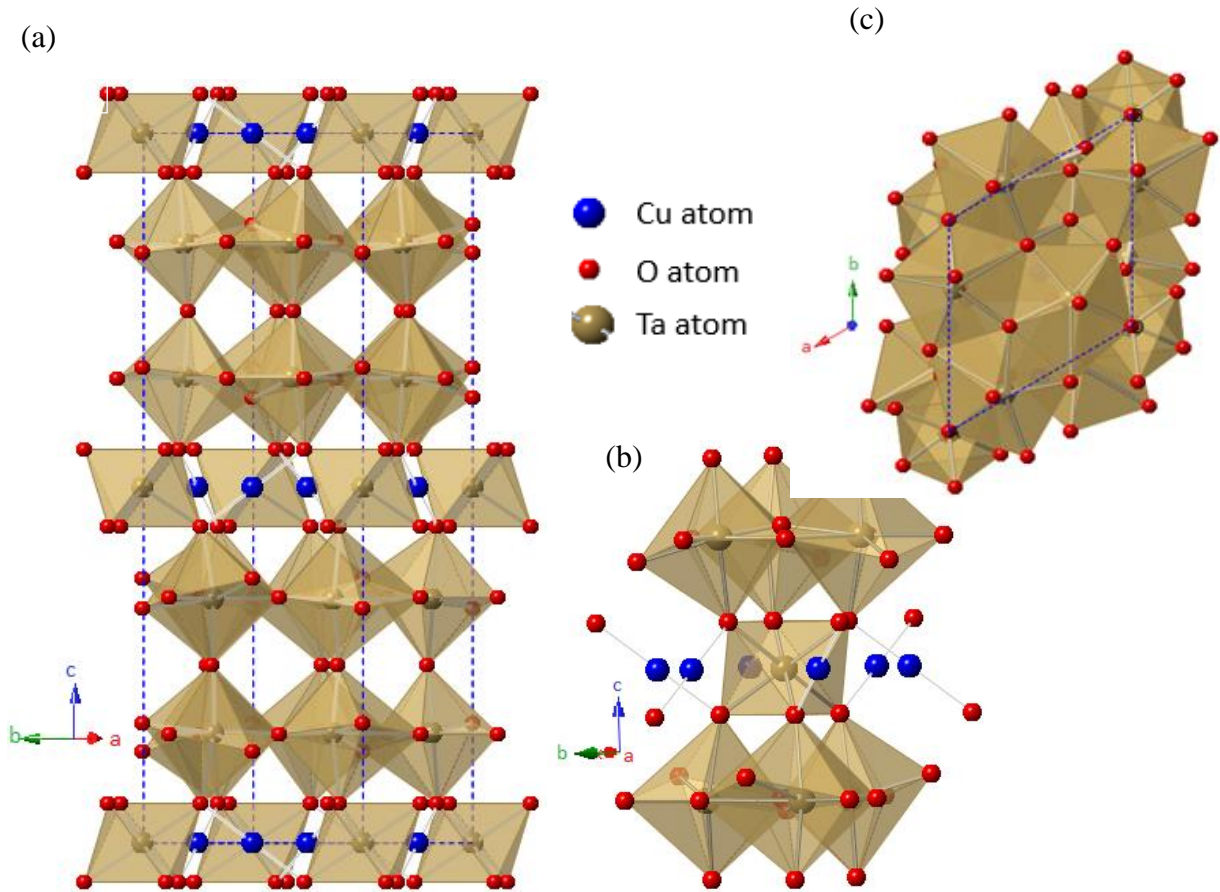


**Figure 3-3.** Crystal structure of Cu<sub>3</sub>Ta<sub>7</sub>O<sub>19</sub> illustrating the (a) the overall unit cell, (b) coordination of the TaO<sub>6</sub> octahedron and (c) edge sharing TaO<sub>7</sub> pentagonal bipyramids.<sup>42</sup>

## Surface Characterization

Results of characterization by scanning Electron Microscopy (SEM) are shown in Figure 3-4 (a and b), and showing micron-sized  $\text{Cu}_3\text{Ta}_7\text{O}_{19}$  crystallites with highly faceted and smooth surfaces. Figures 3-4 (c and d) and 3-5 (a to d) show the results after heating the  $\text{Cu}_3\text{Ta}_7\text{O}_{19}$  crystallites in air at 350 °C for 60 min, 450 °C for 60 min and at 550 °C for 60 min. Interestingly, surface reactions were observed to occur preferentially at the sides and on surface steps of the faces of the hexagonally-shaped particles (e.g., Figure 1C). Increasing temperature and time shows the surface reaction growing in area and size. As recently reported for  $\text{CuNb}_3\text{O}_8$ <sup>59</sup> and  $\text{Cu}_5\text{Ta}_{11}\text{O}_{30}$ <sup>36</sup> phases, heating them in the air results in the formation of CuO nanoislands on the surface which resulted from the extrusion and discrepancy of Cu(I) cations at the surface. Similar results are suggested here for  $\text{Cu}_3\text{Ta}_7\text{O}_{19}$ .

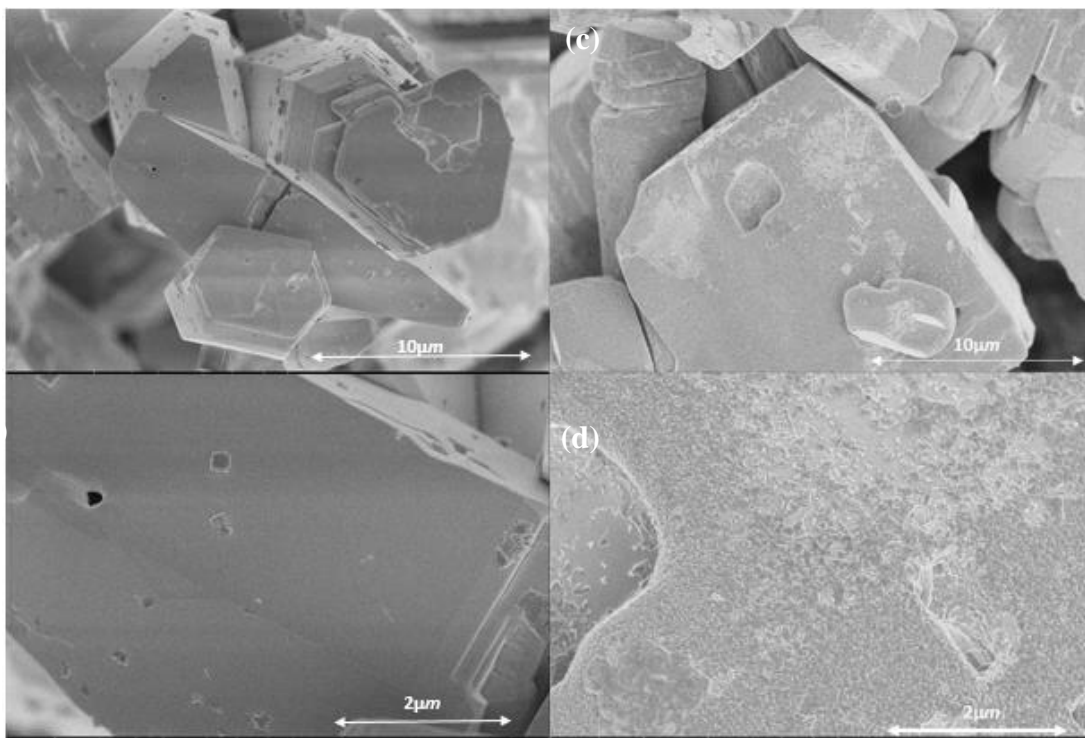


**Figure 3-4.** SEM images of  $\text{Cu}_3\text{Ta}_7\text{O}_{19}$  before heating (a,b), after heating to 350 °C for 60 min (c,d)

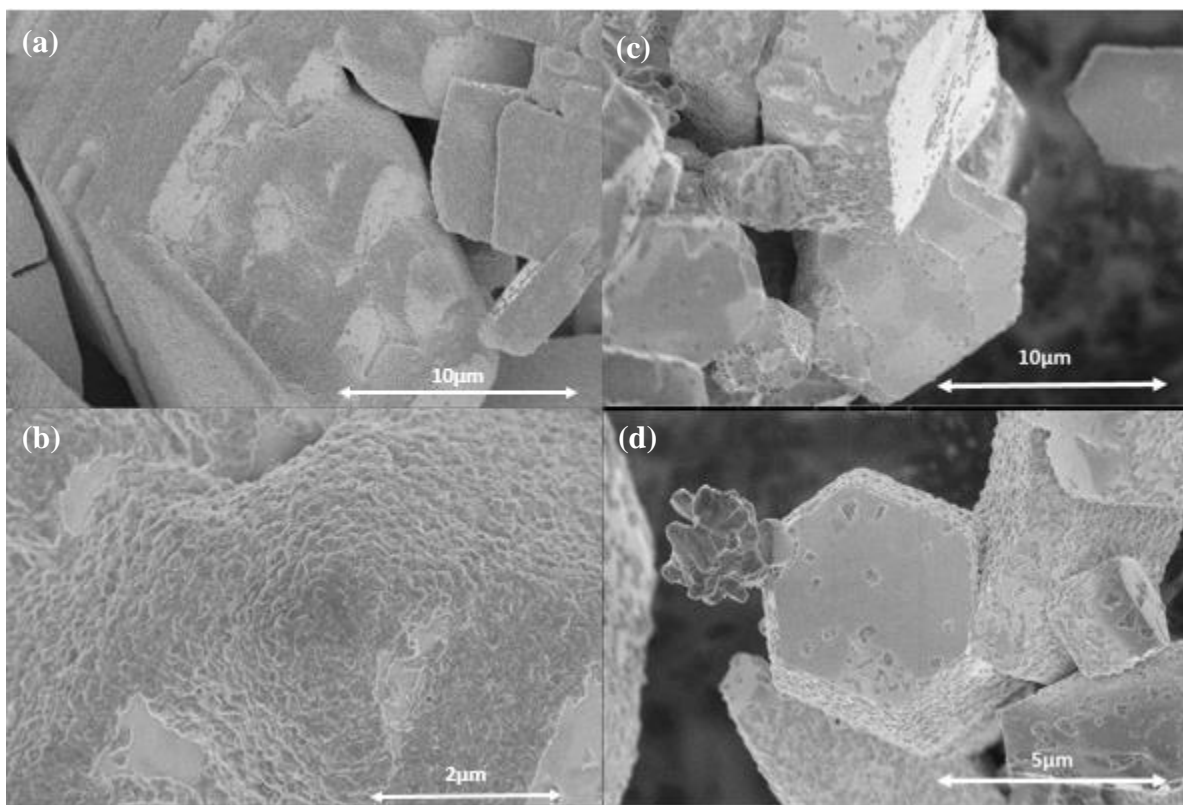


**Figure 3-5.** SEM images of  $\text{Cu}_3\text{Ta}_7\text{O}_{19}$  after heating to 450 °C for 60 min (a,b), after heating to 550 °C for 60 min (c,d)

### Photoelectrochemical Properties

As previously reported, after heating in air to temperatures between 250 and 550°C, polycrystalline films of *p*-type Cu(I) niobates and Cu(I) tantalates irradiated under visible-light exhibit significant increases in their cathodic photocurrents. Some of the phases that have been explored for their photoelectrochemical properties before include  $\text{CuNbO}_3$ ,  $\text{CuNb}_3\text{O}_8$ ,  $\text{Cu}_3\text{Ta}_7\text{O}_{19}$ , and  $\text{Cu}_5\text{Ta}_{11}\text{O}_{30}$ . Among them,  $\text{Cu}_5\text{Ta}_{11}\text{O}_{30}$  has been investigated for the effects of varying heating times and temperatures (in air) of 15, 30, and 60 min on their photoelectrochemical properties. It has been reported that the Cu deficiency in this phase increases with higher heating time and temperature, yielding the increased photocurrents. As

described above for  $\text{Cu}_3\text{Ta}_7\text{O}_{19}$ , similar surface regions of  $\text{CuO}$  were observed for the films heated in air at 350 °C, 450 °C, and 550 °C for increasing times.

Polycrystalline films of  $\text{Cu}_3\text{Ta}_7\text{O}_{19}$  were prepared in order to investigate the relationship between the photoelectrochemical properties and the increasing surface reactions. As shown in Figure 3-6, the polycrystalline films of  $\text{Cu}_3\text{Ta}_7\text{O}_{19}$  shows significantly increased cathodic photocurrents with increases in the heating temperature of the films of 350 °C, 450 °C and 550 °C for 20 minutes, from  $\sim -0.5$  to  $-0.75 \text{ mA/cm}^2$ . Non-oxidized films showed the lowest photocurrent density of about  $\leq -0.1 \text{ mA/cm}^2$ . The highest photocurrent was observed for the film heated at 550 °C for 20 minutes, of  $\sim -0.85 \text{ mA/cm}^2$ . However, shown in Figure 3-7, the chronoamperometry data shows higher photocurrent decay for films heated at the higher temperature range.

The impact of heating time, i.e., for 20, 40, or 60 minutes, on the photoelectrochemical properties was next investigated for the polycrystalline films of  $\text{Cu}_3\text{Ta}_7\text{O}_{19}$ , shown in Figures 3-8 to 3-13. Powder X-ray measurement was carried out for the films after the photoelectrochemical measurements, and showed no detectable impurity phases. The films heated at 350 °C and 450 °C exhibited the greatest increases in photocurrents for increasing heating time. For films heated at 350 °C and 450 °C, the highest photocurrent was observed for the heating time of 60 minutes (Figure 3-8 and 3-10). Contrastingly, films heated at 550 °C showed relatively smaller changes in the photocurrent data. For each film, the chronoamperometric data over 1,000 seconds showed increased photocurrent and decay rates for longer the longer heating times. About 45% photocurrent decay was observed for the film heated to 550 °C, while the films heated to 350 °C and 450 °C heating times showed  $\sim 35\%$  photocurrent decay. For the films heated to 350 °C, increased photocurrent decay is observed for the longer heating time, e.g.,  $\sim 80\%$  decay for 60 min,  $\sim 75\%$  for 40 min, and  $\sim 60\%$  for 20 min, shown in Figure 3-9. A similar trend is exhibited at 450 °C, with the largest photocurrent decay of  $\sim 65\%$  for 60 min, shown in Figure 3-11. Shown in Figure 3-13, heating of the film at 550 °C yields the highest photocurrent decay of 85% after 60 min, compared to a photocurrent decay of 50% for the 20 min heating time. Each of these results is consistent with the

hypothesis that heating the films yields both higher photocurrents as well as poorer stability as a result of the formation of CuO at the  $\text{Cu}_3\text{Ta}_7\text{O}_{19}$  films surfaces.

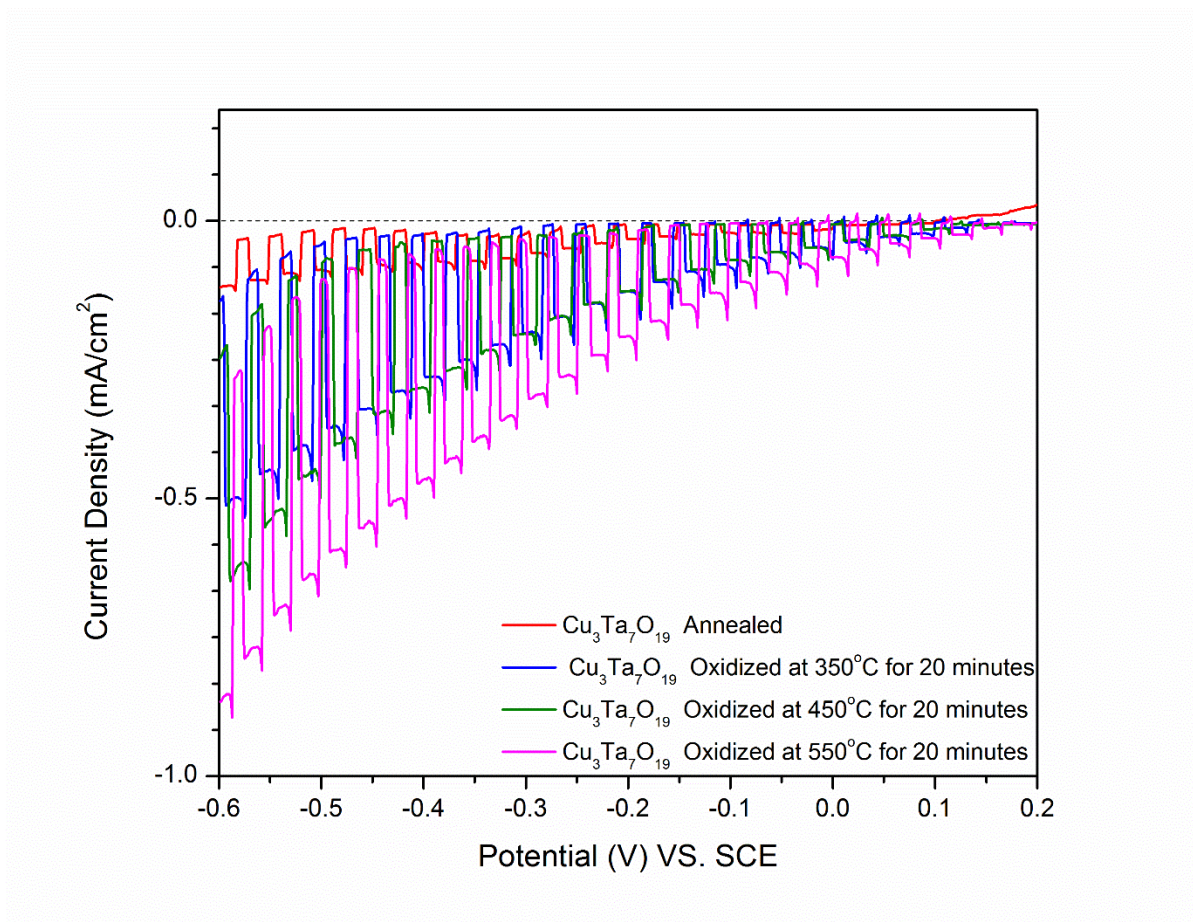


**Figure 3-6.** Current-potential curve in aqueous 0.5M  $\text{Na}_2\text{SO}_4$  solution at pH~6.3 under chopped visible light for  $\text{Cu}_3\text{Ta}_7\text{O}_{19}$  films annealed at 500 °C and no heating in air (red), or heated to 350 °C (blue), 450 °C (green), or 550 °C (magenta).

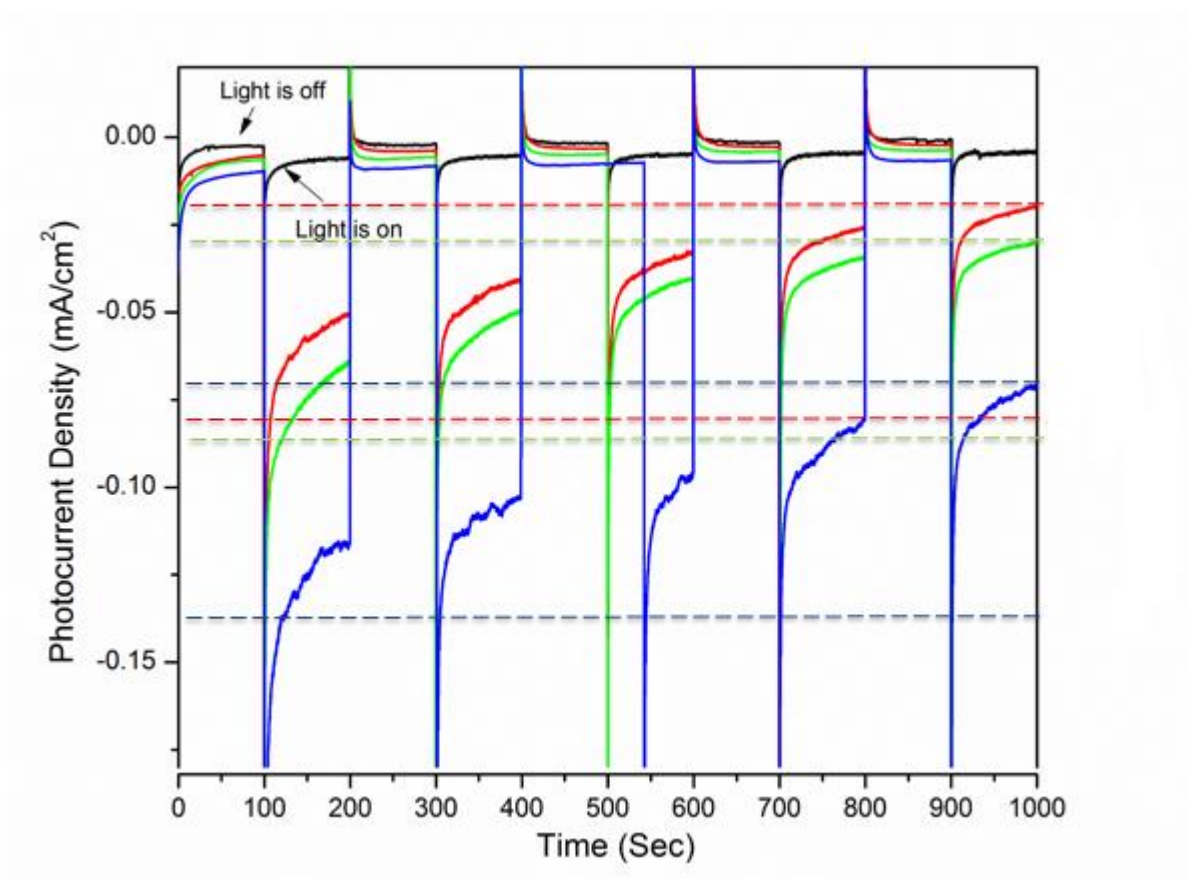


**Figure 3-7.** Chronoamperometry ( $-0.25\text{V}$  applied bias) in aqueous  $0.5\text{M Na}_2\text{SO}_4$  solution at  $\text{pH}\sim 6.3$  under chopped visible light for  $\text{Cu}_3\text{Ta}_7\text{O}_{19}$  films annealed at  $500\text{ }^\circ\text{C}$  and no heating in air (black), or heated in air to  $350\text{ }^\circ\text{C}$  (red),  $450\text{ }^\circ\text{C}$  (green), or  $550\text{ }^\circ\text{C}$  (blue) for 20 minutes.

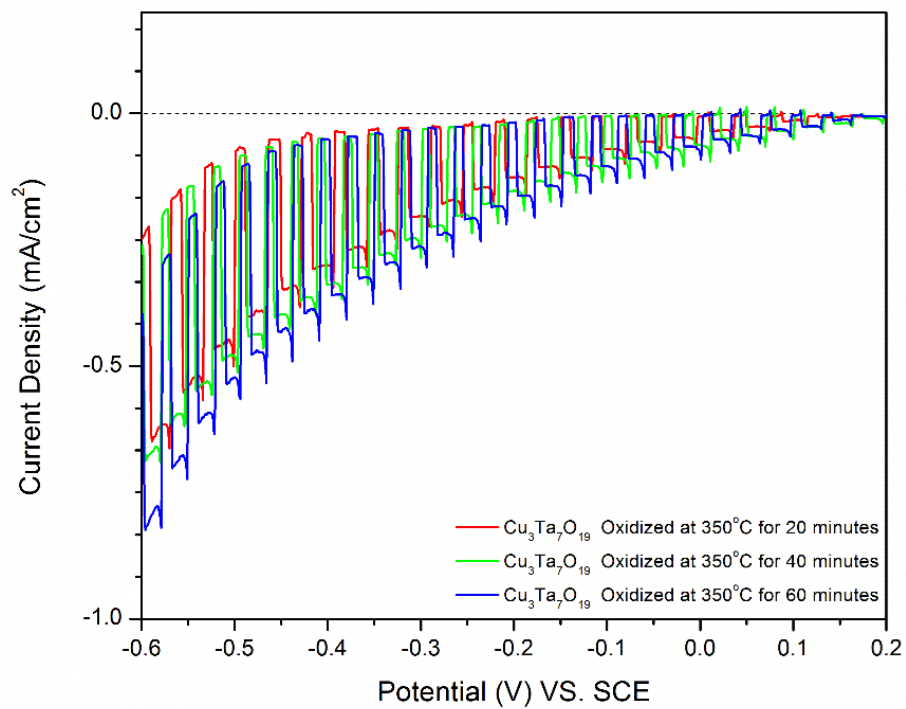


**Figure 3-8.** Current-potential curve in aqueous 0.5M  $\text{Na}_2\text{SO}_4$  solution at pH~6.3 under chopped visible light for  $\text{Cu}_3\text{Ta}_7\text{O}_{19}$  films annealed at 500 °C and heated in air to 350 °C for 20 minutes (red), 40 minutes (green), or 60 minutes (blue).

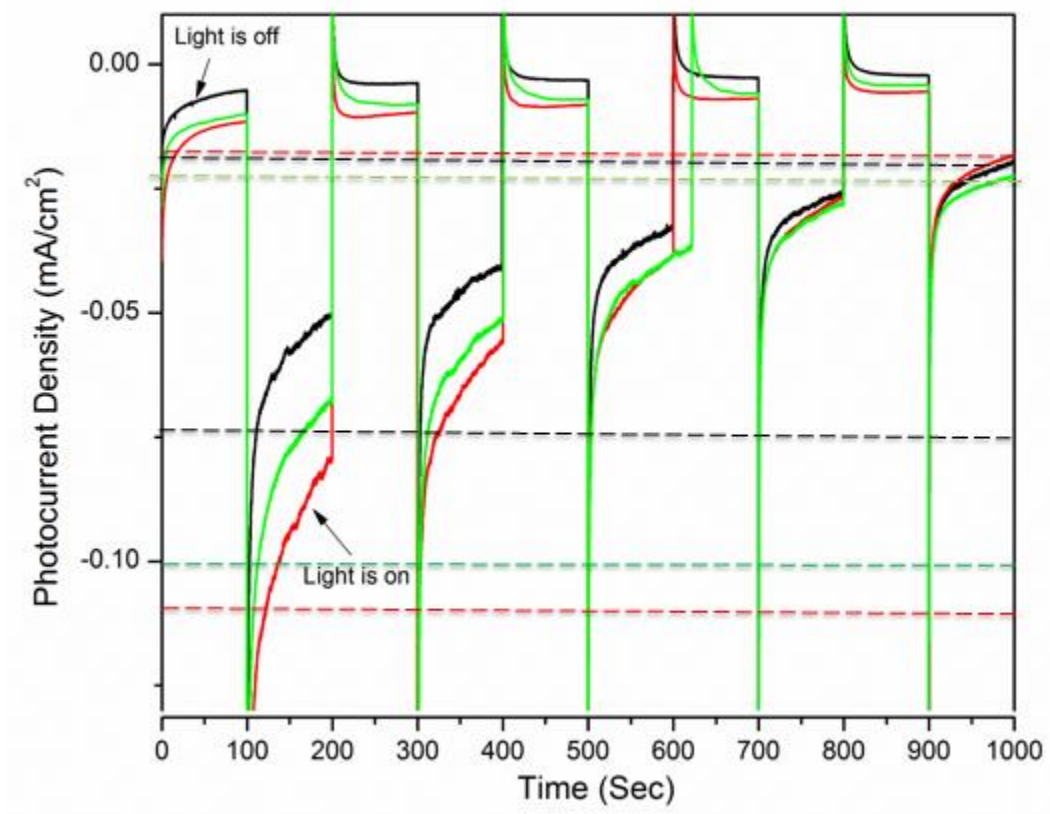


**Figure 3-9.** Chronoamperometry ( $-0.25\text{V}$  applied bias) in aqueous  $0.5\text{M Na}_2\text{SO}_4$  solution at  $\text{pH}\sim 6.3$  under chopped visible light for  $\text{Cu}_3\text{Ta}_7\text{O}_{19}$  films annealed at  $500\text{ }^\circ\text{C}$  and heated in air at  $350\text{ }^\circ\text{C}$  for 20 minutes (black), 40 minutes (green), or 60 minutes (red).

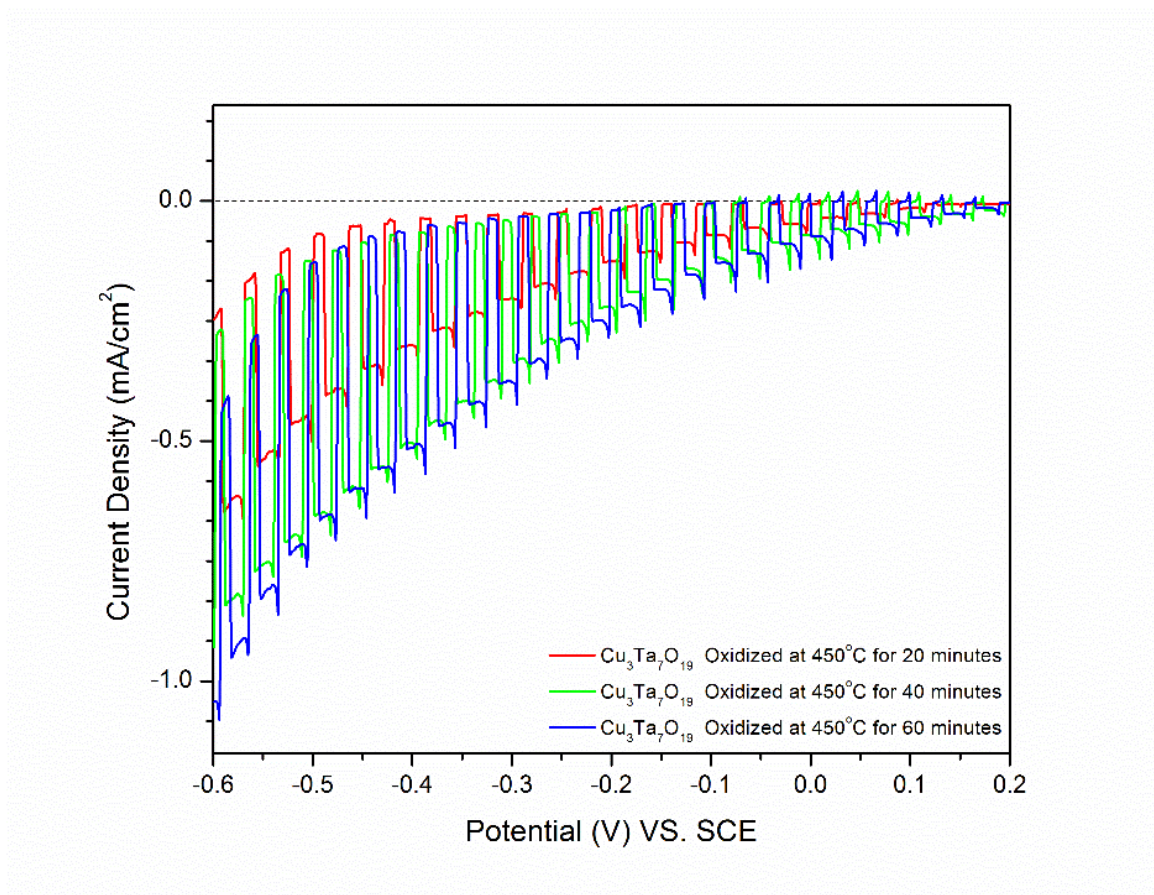


**Figure 3-10.** Current-potential curve in aqueous 0.5M Na<sub>2</sub>SO<sub>4</sub> solution at pH~6.3 under chopped visible light for Cu<sub>3</sub>Ta<sub>7</sub>O<sub>19</sub> films annealed at 500 °C and heated in air at 450 °C for 20 minutes (red), 40 minutes (green), or 60 minutes (blue).

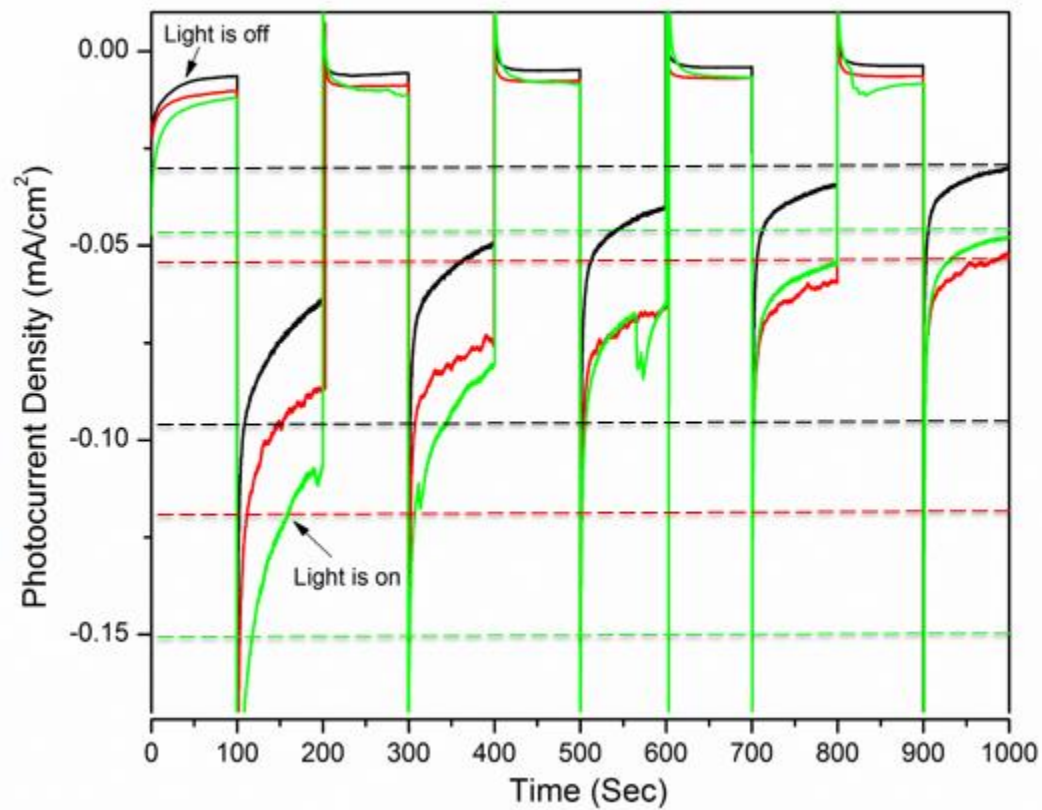


**Figure 3-11.** Chronoamperometry ( $-0.25\text{V}$  applied bias) in aqueous  $0.5\text{M Na}_2\text{SO}_4$  solution at  $\text{pH}\sim 6.3$  under chopped visible light for  $\text{Cu}_3\text{Ta}_7\text{O}_{19}$  films annealed at  $500\text{ }^\circ\text{C}$  and heated in air at  $450\text{ }^\circ\text{C}$  for 20 minutes (black), 40 minutes (red), or 60 minutes (green).

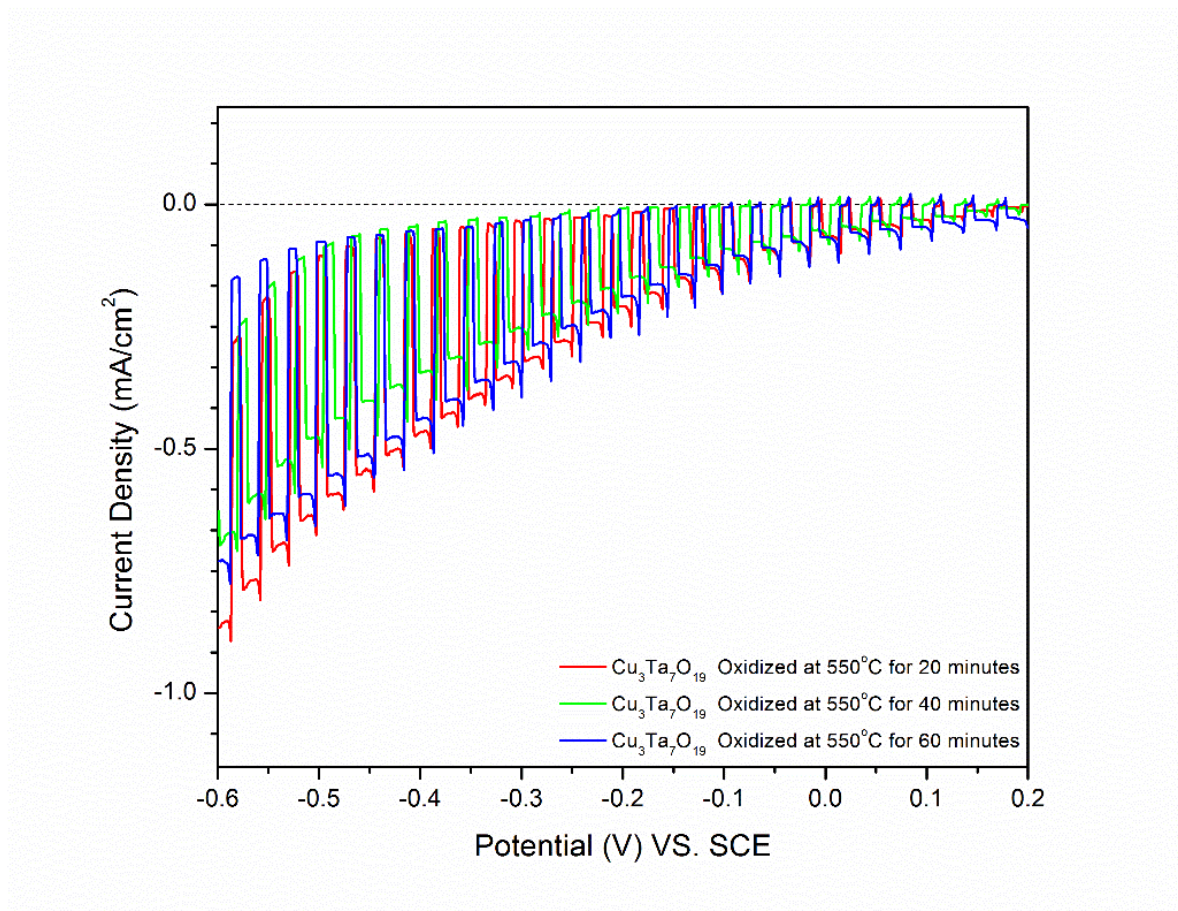


**Figure 3-12.** Current-potential curve in aqueous 0.5M  $\text{Na}_2\text{SO}_4$  solution at pH~6.3 under chopped visible light for  $\text{Cu}_3\text{Ta}_7\text{O}_{19}$  films annealed at 500 °C and heated in air at 550 °C for 20 minutes (red), 40 minutes (green), or 60 minutes (blue).

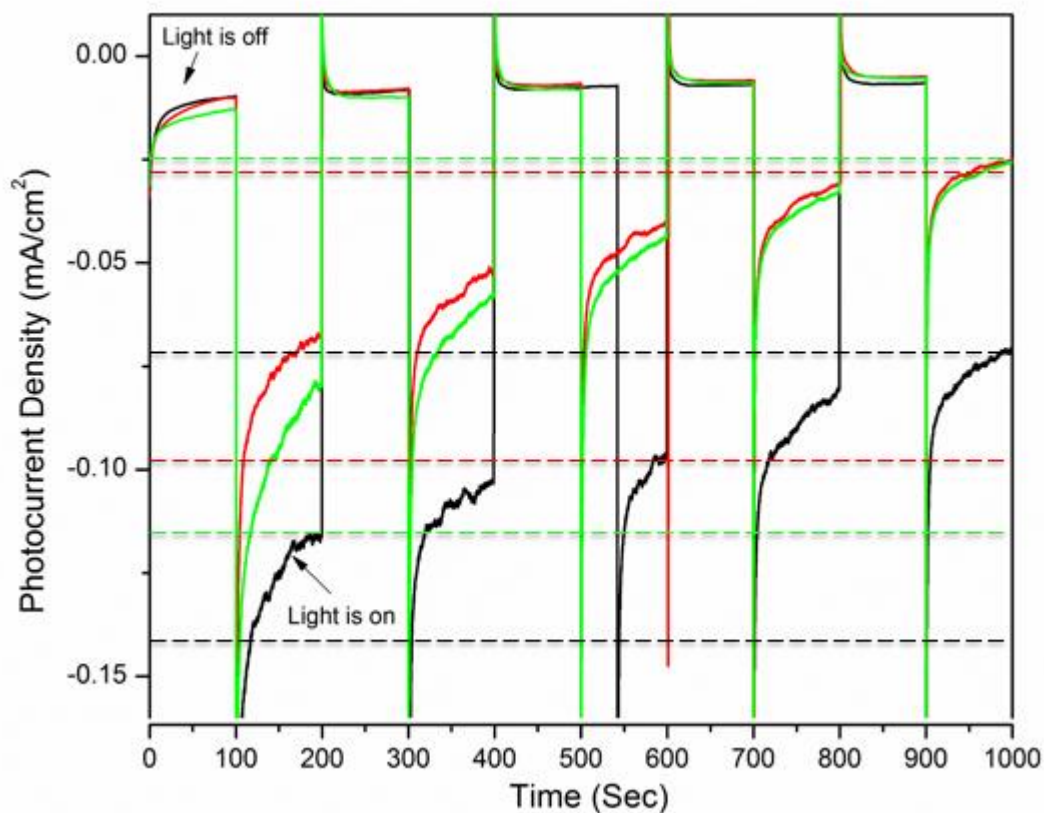


**Figure 3-13.** Chronoamperometry ( $-0.25\text{V}$  applied bias) in aqueous  $0.5\text{M Na}_2\text{SO}_4$  solution at  $\text{pH}\sim 6.3$  under chopped visible light for  $\text{Cu}_3\text{Ta}_7\text{O}_{19}$  films annealed at  $500\text{ }^\circ\text{C}$  and heated in air at  $550\text{ }^\circ\text{C}$  for 20 minutes (black), 40 minutes (red), or 60 minutes (green).

### **Lattice Refinements from Powder X-ray Diffraction Data**

Films of  $\text{Cu}_3\text{Ta}_7\text{O}_{19}$  heated in air at  $350\text{ }^\circ\text{C}$  were analyzed by powder XRD after the chronoamperometry measurements. As the heating time of the film increases, the photocurrent is observed to increase. However, the highest photocurrent density observed for the film heated to 60 min, shown in Figure 3-8, suggests there is an optimum heating time for the film. No impurities were observed after  $350\text{ }^\circ\text{C}$  oxidation of the films. However, the powder XRD data

show peak shifting to smaller  $2\theta^\circ$  values in the 26-32  $2\theta^\circ$  range, Figure 3-14, indicative of a larger unit cell and perhaps consistent with copper migration out of the structure. Shown in Figure 3-15, increases in the  $a/b$  lattice parameter and volume of the unit cell. These data are also listed in Tables 3-1 and 3-2. The increases in the unit cell parameters  $a/b$  and unit cell volume is the opposite of what has been observed for  $\text{Cu}_5\text{Ta}_{11}\text{O}_{30}$  during extrusion of Cu(I) out of the crystalline structure. Further characterization of the composition of the crystalline structure as a function of heating time and temperature is necessary in order to understand this effect.

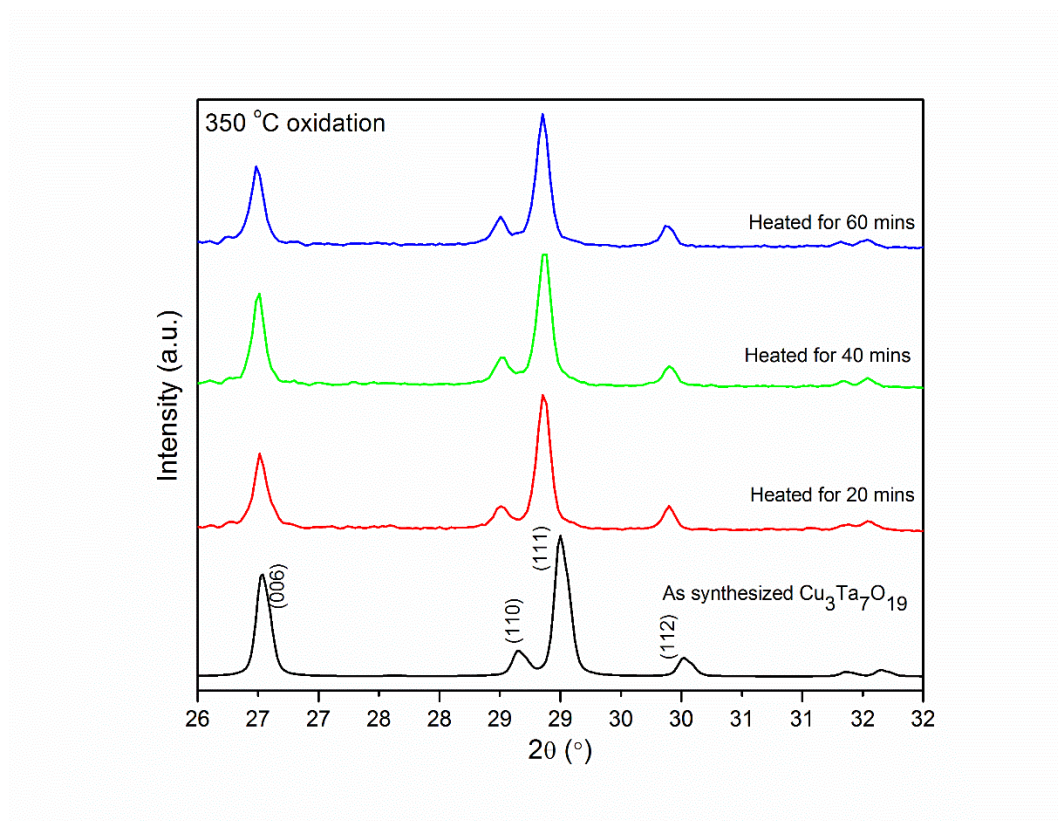
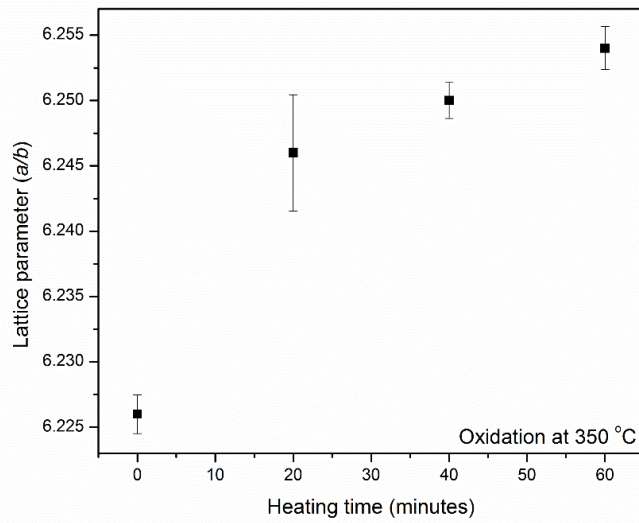


**Figure 3-14.** Powder XRD patterns of  $\text{Cu}_3\text{Ta}_7\text{O}_{19}$  between  $26^\circ$  and  $32^\circ$  after heating to 350 °C for 20 minutes, 40 minutes, and 60 minutes.

(a)



(b)

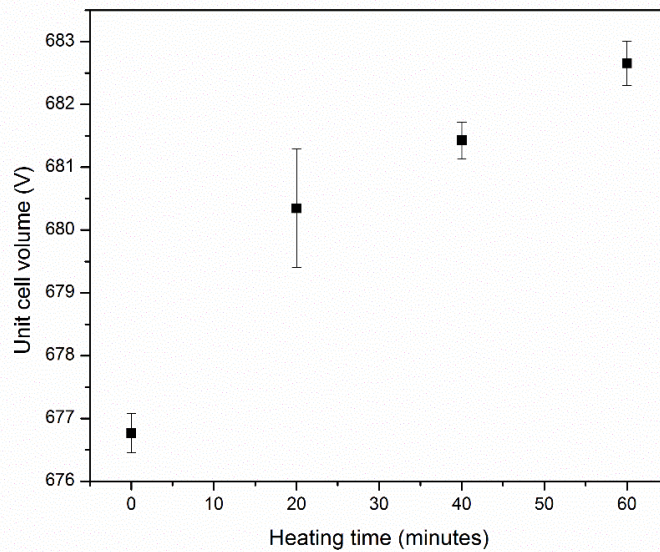


**Figure 3-15.** Refined lattice parameters of  $\text{Cu}_3\text{Ta}_7\text{O}_{19}$  after heating to 350 °C for 20 minutes, 40 minutes and 60 minutes. The upper graph (a) is a plot of the *a/b* lattice constants and the lower graph the unit cell volume (b), with error bars indicating estimated standard deviations.

**Table 3-1.** Lattice constants, and volumes from cell refinement after 450°C oxidations.

450 °C Oxidation					
Time (min)	<i>a</i>	<i>b</i>	<i>c</i>	Volume (Å <sup>3</sup> )	Δ Volume
0	6.226(1)	6.226(1)	20.159(7)	676.766	0
20	6.253(1)	6.253(1)	20.120(7)	681.4687	4.693
40	6.257(2)	6.257(2)	20.15(1)	683.3595	6.585
60	6.261(1)	6.261(1)	20.161(9)	684.6165	7.841

**Table 3-2.** Lattice constants, and volumes from cell refinement after 550°C oxidations.

550 °C Oxidation					
Time (min)	<i>a</i>	<i>b</i>	<i>c</i>	Volume (Å <sup>3</sup> )	Δ Volume
0	6.226(1)	6.226(1)	20.159(7)	676.766	0
20	6.256(1)	6.256(1)	20.055(6)	679.779	3.003
40	6.26(1)	6.26(1)	20.13(5)	684.780	8.004
60	6.27(1)	6.27(1)	20.13(6)	686.770	9.994

## Conclusion

The molten-flux synthesis method was used to prepare the previously reported  $\text{Cu}_3\text{Ta}_7\text{O}_{19}$ .<sup>37,47</sup> The photoelectrochemical properties of its polycrystalline films were investigated as a function of the heating conditions, i.e., heated to 350 °C, 450 °C or 550 °C for 20 minutes, 40 minutes, or 60 minutes. Increased photocurrents were observed for the films heated in the air for longer heating times and higher heating temperatures. Heating of the films resulted in an increase in the unit cell volume of  $\text{Cu}_3\text{Ta}_7\text{O}_{19}$ , and concomitantly, a surface reaction was detectable via SEM images. Future experiments are necessary, i.e., Rietveld refinements, and TEM and XPS investigations, in order to better understand the relationship to the photoelectrochemical properties of the material.

## CHAPTER 4

### SOLID SOLUTIONS OF $\text{Cu}_3(\text{Ta}_{1-x}\text{Nb}_x)_7\text{O}_{19}$ ( $x \leq 0.15$ ): IMPACT OF Nb(V) SUBSTITUTION ON ITS STRUCTURE, BANDGAP SIZES AND PHOTOELECTROCHEMICAL PROPERTIES

#### Introduction

Solid solutions have been investigated for the discovery of new types of visible-light absorbing photocatalysts.<sup>42,46</sup> Solid solutions can be used to tune the band gaps of metal oxides, thus enabling their potential absorption of photon energies across the solar spectrum. By tuning the valance and/or conduction band positions, these could then be suitably located with respect to important redox couples and more efficient photocatalysts could be achieved.<sup>48</sup> A solid solution means the substitution of one element for another in a disordered arrangement in a crystalline solid. Several semiconducting solid solutions are reported to be active in photocatalytic reactions in the absence of noble metal cocatalysts. Among them,  $\text{Cd}_{1-x}\text{Zn}_x\text{S}$  and  $(\text{Ga}_{1-x}\text{Zn}_x)(\text{N}_{1-x}\text{O}_x)$  solid solutions have been intensely investigated because of their visible-light bandgap sizes and high photocatalytic activity for hydrogen production reaction under visible light illumination.<sup>47,49</sup> Recent research in the Maggard group has uncovered the  $\text{LiNb}_3\text{O}_8\text{-CuNb}_3\text{O}_8$ ,<sup>37</sup>  $(\text{Na}_{1-x}\text{Cu}_x)_2\text{Ta}_4\text{O}_{11}$ ,<sup>50</sup>  $\text{NaCu}(\text{Ta}_{1-x}\text{Nb}_x)_4\text{O}_{11}$ <sup>37</sup> and  $\text{Cu}_5(\text{Ta}_{1-x}\text{Nb}_x)_{11}\text{O}_{30}$ <sup>51</sup> solid solutions that were investigated for the impact of changes in their crystalline structures and compositions on their bandgap sizes and photoelectrochemical and photocatalytic properties. For example, replacement of the alkali metals lithium and sodium by Cu(I) cations, and/or the substitution of Nb(V) cations for Ta(V) cations, can significantly decrease the band gap sizes of these *p*-type semiconducting oxides by up to ~1.0 to ~2.0eV. As reported for  $\text{LiNb}_3\text{O}_8\text{-CuNb}_3\text{O}_8$ , increasing the substitution of Li (I) by Cu(I) results in a new higher-energy valence band.<sup>46</sup> Conversely, an increasing substitution of Nb (V) cations reduces the conduction band energy owing to the lower energy *4d*-orbitals of Nb in comparison to the higher energy *5d*-orbitals of Ta.<sup>37,51</sup> However, relatively little is currently known regarding the impact of solid solution compositions on their photoelectrochemical properties as polycrystalline films.

As previously reported, polycrystalline films of  $\text{Cu}_3\text{Ta}_7\text{O}_{19}$  show high cathodic photocurrents ( $\sim 1\text{-}1.5\text{mA/cm}^2$ ) under visible light irradiation. This semiconductor has a band gap size of  $\sim 2.5\text{eV}$  and band energies suitable for driving the water splitting reaction. Reported herein are the syntheses of members of a new  $\text{Cu}_3(\text{Ta}_{1-x}\text{Nb}_x)_7\text{O}_{19}$  solid solution and an investigation of the effect of the Nb(V) content on the conduction-band energy, as well as its optical and photoelectrochemical properties.

## **Experimental**

### **Materials**

The reagents were used as purchased without any further modification. The reactants were reagent grade  $\text{Ta}_2\text{O}_5$  (Alfa Aesar, min 99.99%),  $\text{Cu}_2\text{O}$  (Alfa Aesar, 99.99%),  $\text{Nb}_2\text{O}_5$  (Alfa Aesar, 99.99%) and  $\text{CuCl}$  (Alfa Aesar, 99.99%). For the photoelectrochemical measurements,  $\text{Na}_2\text{SO}_4$  (Alfa Aesar, 99.0%),  $\text{NaOH}$  (>97%, Fisher Scientific), and deionized water were used.

### **Synthesis**

The molten-salt flux method was used by combining the appropriate stoichiometric mixtures of  $\text{Cu}_2\text{O}$ ,  $\text{Nb}_2\text{O}_5$  and  $\text{Ta}_2\text{O}_5$  together with the  $\text{CuCl}$  as the flux in a 10:1 molar ratio. This reaction mixture was ground in a mortar and pestle for around 30 minutes to a homogenous powder in an argon atmosphere in a glovebox. The reactant mixtures were loaded into a cleaned quartz tube and flame sealed on a vacuum line. Different elements of the solid solutions were heated for different temperatures and for different time periods in order to get a phase pure product according to powder XRD. The  $\text{CuCl}$  flux and any unreacted  $\text{Cu}_2\text{O}$  was washed out from the products by using aqueous 0.5M  $\text{NaOH}$  several times, and subsequently with deionized water. The washed product was dried in the oven at  $\sim 80^\circ\text{C}$ .

## Characterization

### X-ray Diffraction Techniques

The reaction products were characterized by powder X-ray diffraction techniques (INEL, Cu  $K\alpha_1$   $\lambda = 1.54056 \text{ \AA}$ , CPS120 detector). To obtain diffractograms a curved position sensitive detector (CPS-120) was used in transmission mode. Two pieces of Scotch tape was used with a sample mass of  $\sim 50 \text{ mg}$  placing in between them and rotated between the X-ray beam and detector. The data collection time was anywhere from 30 to 90 min. The experimental patterns were compared to the calculated XRD pattern of  $\text{Cu}_3\text{Ta}_7\text{O}_{19}$ . The experimental lattice parameters were refined using the LATCON software program. Around 10 prominent XRD peaks per pattern were selected for the refinements.

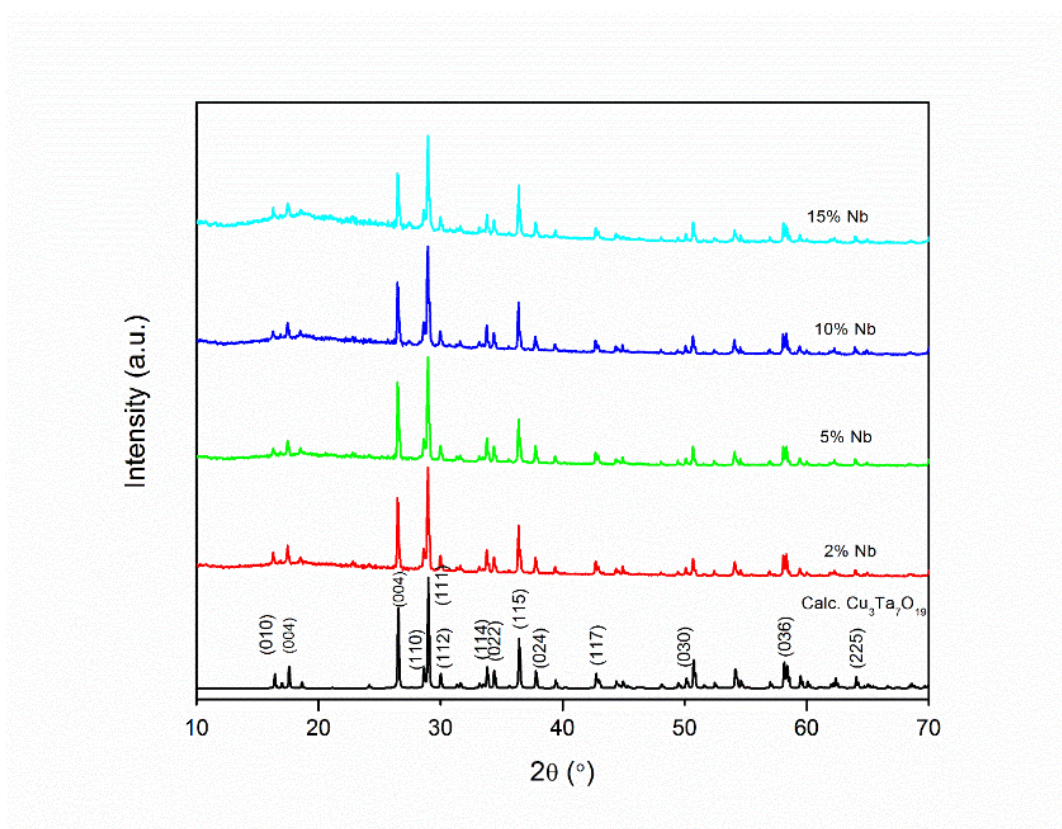


**Figure 4-1.** The indexed powder X-ray diffraction pattern of  $\text{Cu}_3\text{Ta}_7\text{O}_{19}$ , including both experimental (top three) and calculated (bottom).

## Optical Properties

The UV-Visible Diffuse Reflectance Spectra (DRS) were collected on a Shimadzu UV-3600. Approximately 30mg of sample was mounted to a BaSO<sub>4</sub> pressed plate and placed along the external window. Pressed BaSO<sub>4</sub> plates were used as a reference and the data were plotted as the remission function as  $F(R_{\infty}) = (1 - R_{\infty})^2 / (2R_{\infty})$ , based on the Kubelka-Munk theory of diffuse reflectance which relates reflectance, R, to an absorption coefficient  $\alpha$  and a scattering coefficient, s.<sup>41</sup> The wavelength is converted to photon energy by using the formula  $eV = 1240/\lambda$  and the band gap is estimated from the linear rise in the absorbance.

## Photoelectrochemical Measurements

Polycrystalline films were prepared on TEK-15 fluorine-doped tin oxide (FTO) slides. After sonication of the FTO slides in deionized water, ethanol and acetone were used for 30 minutes each and the films dried in air at room temperature. On the FTO, an ~1cm<sup>2</sup> area was taped off on the conducting side using Scotch 3M tape, and the drop casting and doctor blade method was used to deposit the material on the slide. A water/tert-butanol solution was used as the dispersant. The tape was removed after the sample dried. These films were then annealed at 500°C for 3 hours under dynamic vacuum. After annealing the films, these were either used as is for photoelectrochemical measurements or were heated in air for different times and temperatures. Polycrystalline films of Cu<sub>3</sub>Ta<sub>7</sub>O<sub>19</sub> were examined in a photoelectrochemical cell for measurement of the current density and photostability using 0.5M Na<sub>2</sub>SO<sub>4</sub> solution as electrolyte and at pH of ~6.3.

## Thermogravimetric Analysis

The thermal stability and decomposition of Cu<sub>3</sub>Ta<sub>7</sub>O<sub>19</sub> were measured on a TA Instruments SDT2960 simultaneous DSC-TGA under flowing nitrogen gas by heating to 450 °C at a programmed rate of 30 °C/min. A weighed amount (35–45mg) was loaded onto a pan, equilibrated and tared at room temperature, and the data plotted as time (min) versus weight gain percentages.

## Results and Discussions

### Crystal Structure

The structure of  $\text{Cu}_3\text{Ta}_7\text{O}_{19}$  is comprised of linearly coordinated Cu(I) cations within  $\text{CuO}_2$  layers and edge-sharing pentagonal bipyramidal  $\text{TaO}_7$  double layers, with intervening  $\text{TaO}_6$  octahedra.<sup>50</sup> This type of structure has been described as part of a family of structures similar to the  $\alpha\text{-U}_3\text{O}_8$  structure type.<sup>32</sup> This member of this family contains alternating single  $\text{TaO}_6$  octahedra and double layers of the  $\text{TaO}_7$  pentagonal bipyramids. Six linearly coordinated Cu(I) cations are surrounding each  $\text{TaO}_6$  octahedron.

A related member of the Cu(I)-tantalate family,  $\text{Cu}_5\text{Ta}_{11}\text{O}_{30}$ ,<sup>36</sup> contains alternating single and double layers of the  $\text{TaO}_7$  pentagonal bipyramids. Each of these is separated by layers of  $\text{TaO}_6$  octahedra and nearly linearly coordinated Cu(I) cations. By contrast, the  $\text{Cu}_2\text{Ta}_4\text{O}_{11}$  structure<sup>52</sup> contain single, double, or a combination of layers of edge-shared  $\text{TaO}_7$  pentagonal bipyramids that alternate with layers of isolated  $\text{TaO}_6$  octahedral surrounded by the Cu(I) cations.

Compared to the parent phase  $\text{Cu}_3\text{Ta}_7\text{O}_{19}$ , there is relatively little to no detectable peak shifting in the powder XRD data for different members of the solid solution  $\text{Cu}_3(\text{Ta}_{1-x}\text{Nb}_x)_7\text{O}_{19}$ . The unit cell lattice parameters and unit cell volume of the  $\text{Cu}_3(\text{Ta}_{1-x}\text{Nb}_x)_7\text{O}_{19}$  solid was refined from the powder XRD data as a function of the composition, shown in Figures 4-3 and 4-4. These data indicate that with an increasing amount of Nb(V) substitution into the structure the lattice parameters initially increase and then stay constant. However, both Ta(V) and Nb(V) have very similar Shannon radii for octahedral and pentagonal bipyramidal coordination environments. Thus, the structure of  $\text{Cu}_3(\text{Ta}_{1-x}\text{Nb}_x)_7\text{O}_{19}$  contains a random mixture of Nb(V) and Ta(V) cations on the same structural sites.

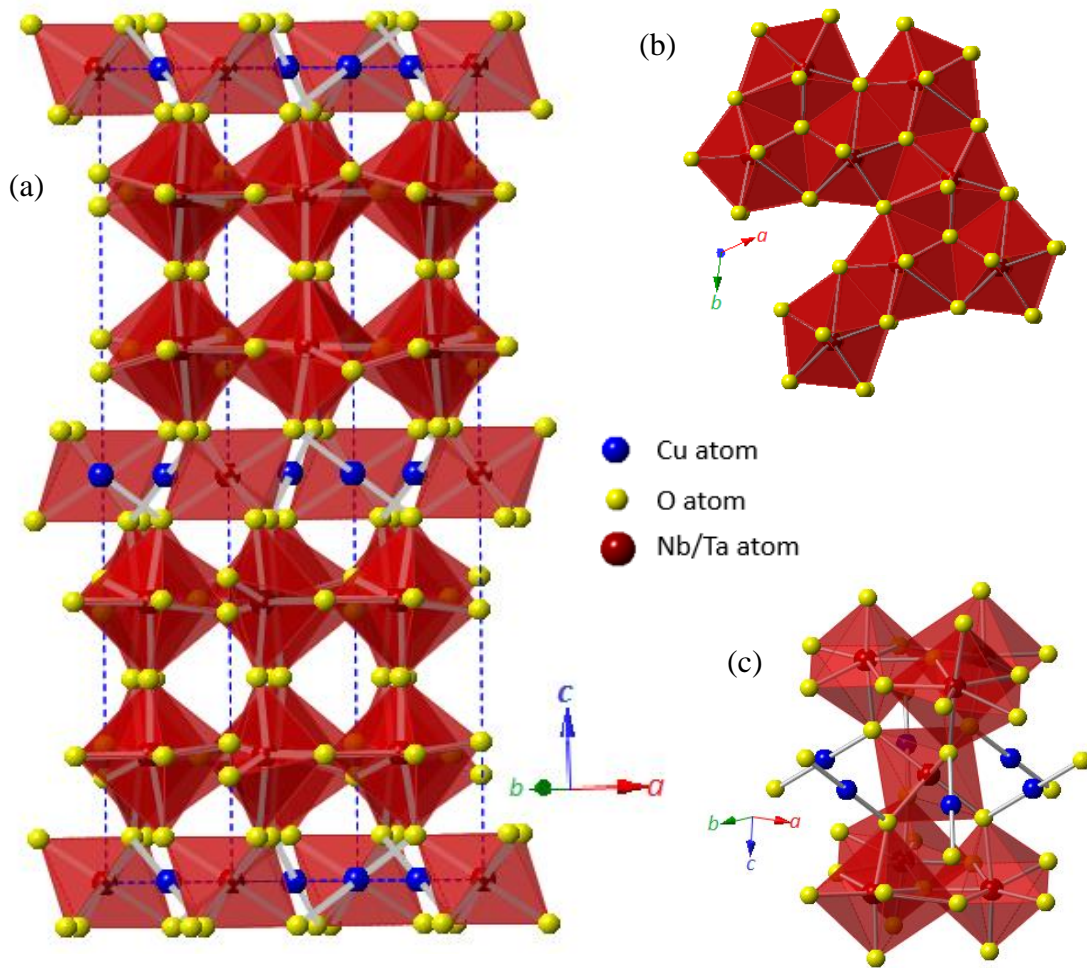


**Figure 4-2.** Crystal structure of  $\text{Cu}_3(\text{Ta}_{1-x}\text{Nb}_x)_7\text{O}_{19}$ , illustrating (a) the overall unit cell, (b) the edge sharing  $\text{TaO}_7$  pentagonal bipyramids, and (c) coordination of the  $\text{TaO}_6$  octahedron.

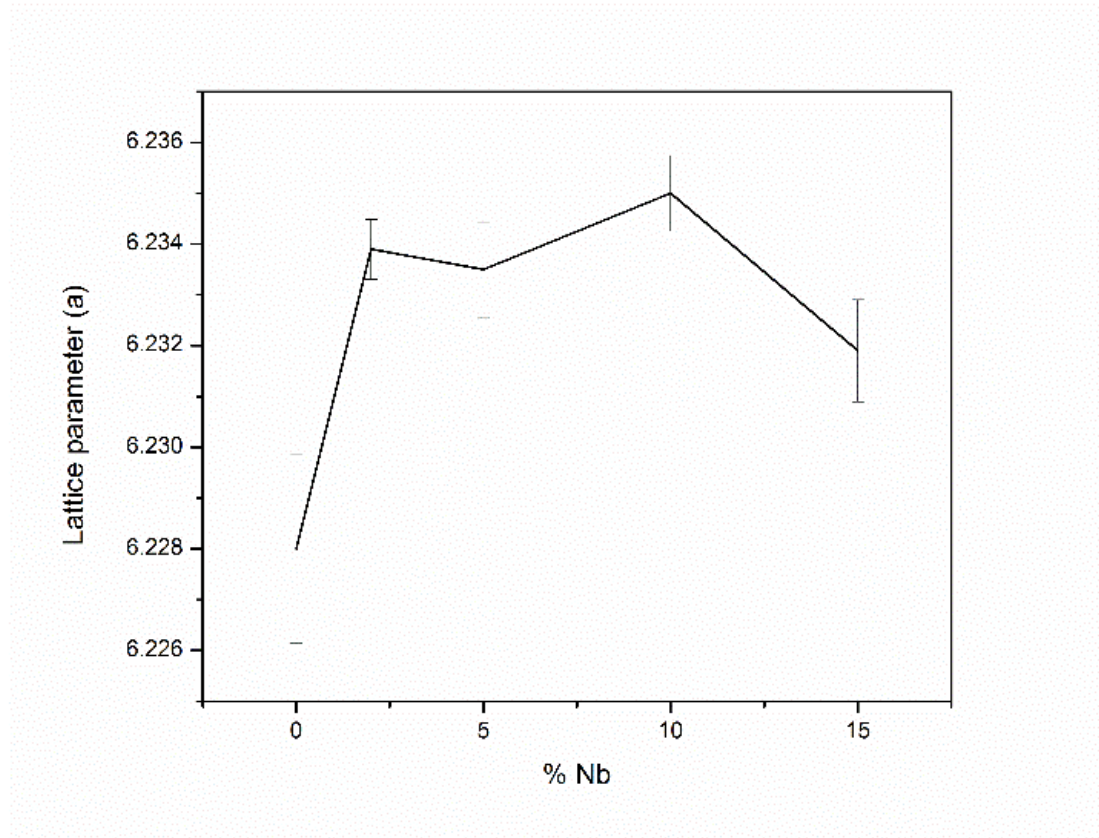


**Figure 4-3.** Refined *a/b* lattice parameters of  $\text{Cu}_3(\text{Ta}_{1-x}\text{Nb}_x)_7\text{O}_{19}$  ( $0 < x \leq 0.15$ ) as a function of Nb content.

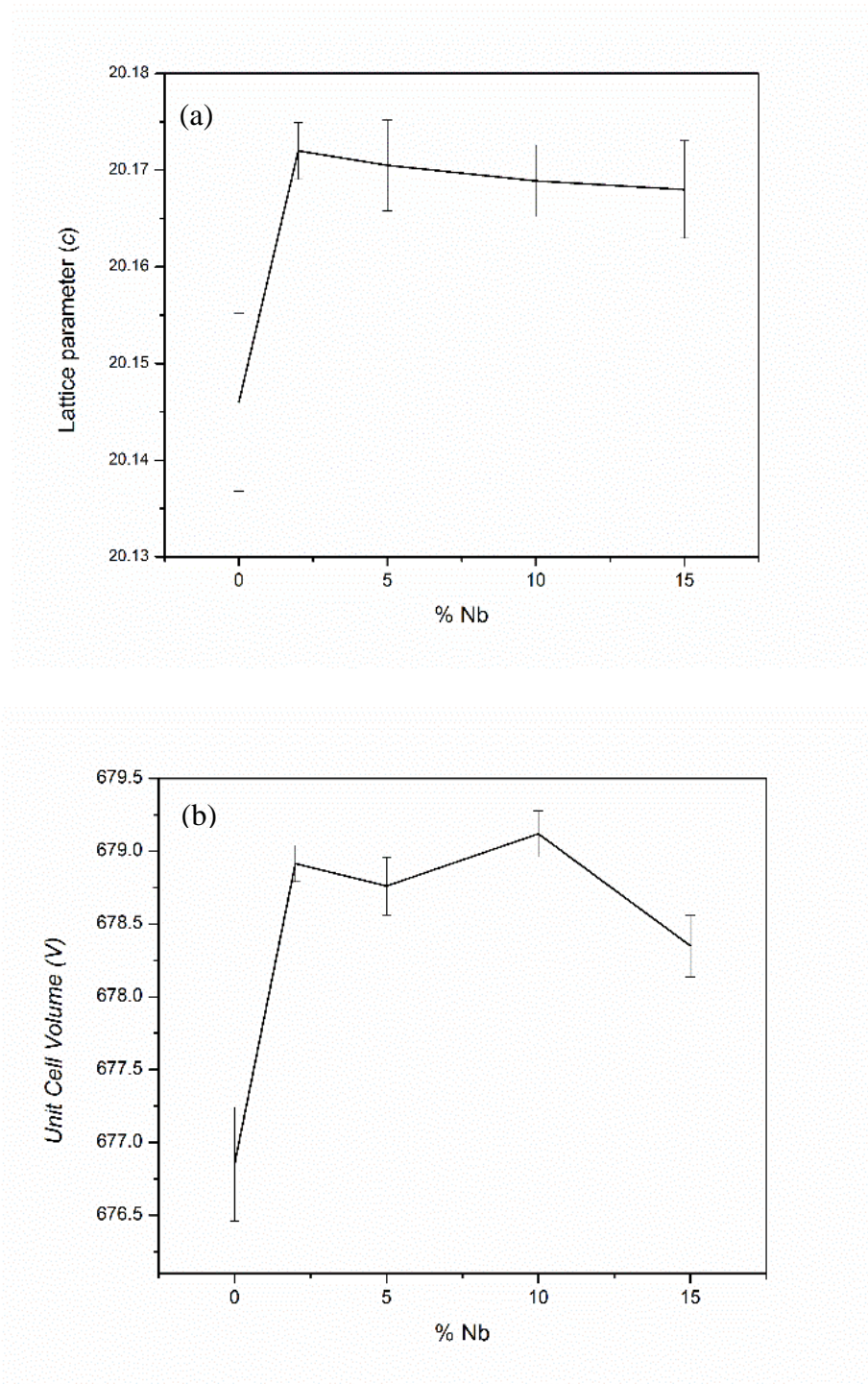


**Figure 4-4.** Refined c lattice parameter (a) and unit cell volume (b) of  $\text{Cu}_3(\text{Ta}_{1-x}\text{Nb}_x)_7\text{O}_{19}$  ( $0 < x \leq .15$ ) as a function of Nb content.

## Optical Properties

Previously reported,<sup>61</sup> pure  $\text{Cu}_3\text{Ta}_7\text{O}_{19}$  is bright yellow colored and has a band gap size of  $\sim 2.5\text{eV}$  and its valence and conduction band edges are composed of filled Cu  $3d^{10}$  and empty Ta  $5d^0$  orbitals respectively. As Ta(V) cations are substituted for by Nb(V) in the solid solution, the color of the material changes to red, indicating a red shifting of the band gap size. Shown in Figure 4-5, the UV-Vis diffuse reflectance spectroscopy measurements of the solid solution also show a noticeable red shift in the direct and indirect band gap transitions. In the solid solution  $\text{Cu}_3(\text{Ta}_{1-x}\text{Nb}_x)_7\text{O}_{19}$  ( $0 < x \leq 0.15$ ), the direct bandgap decreases from  $\sim 2.5$  to  $\sim 2.1$  eV and the indirect bandgap decreases from  $\sim 2.3$  to  $\sim 1.8$  eV. The redshift of the bandgap size is hypothesized to result from the lower energy  $d$ -orbitals of the Nb(V) cations, and resulting in a lower-energy conduction band. The red shift of the bandgap size of the solid solution thus enables a broader possible absorption of sunlight. Further investigations are necessary to understand the origins of the red shifting of its band gap size.

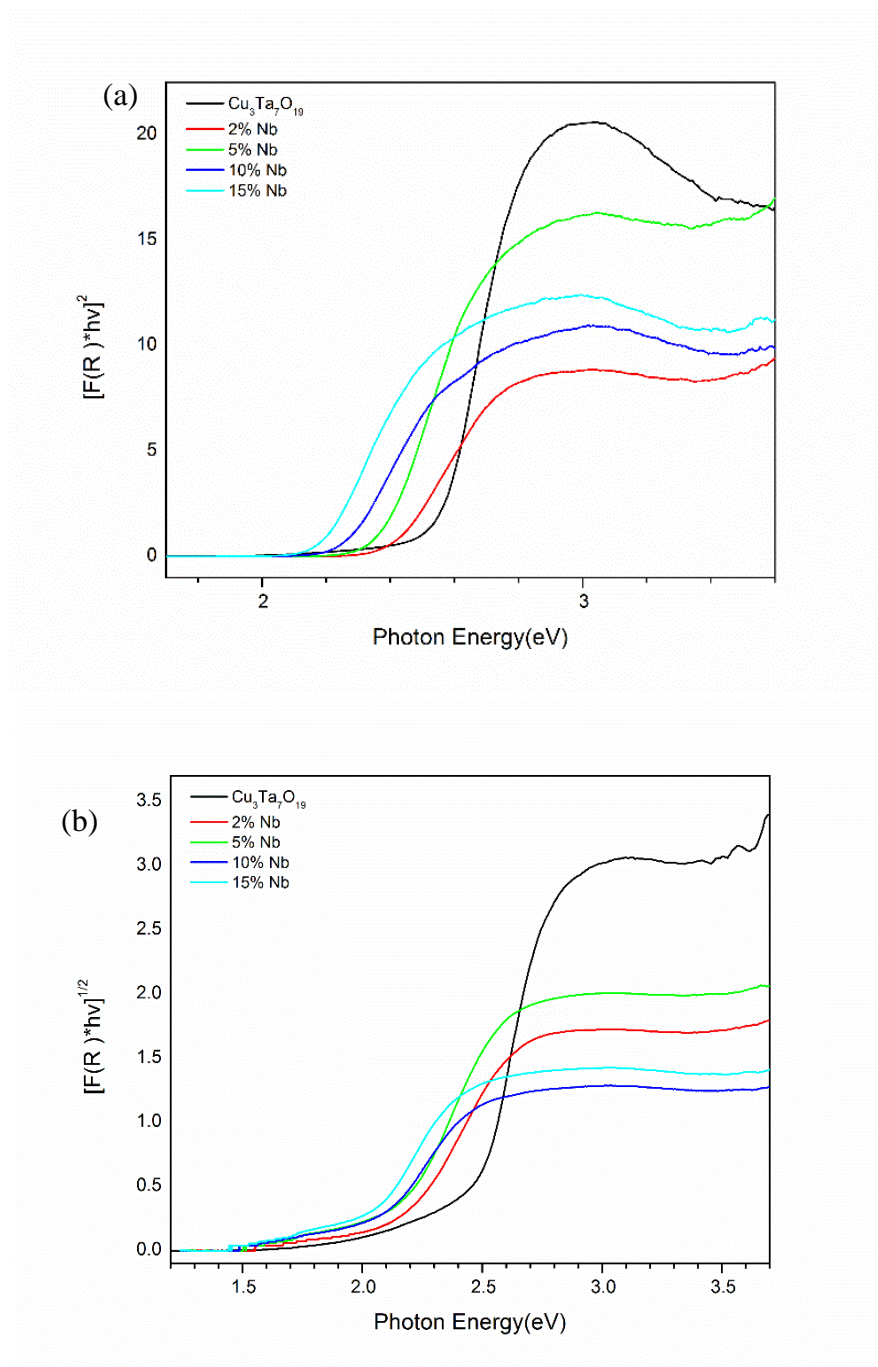


**Figure 4-5.** Tauc plots of the direct (a) and indirect (b) band gap transitions of the  $\text{Cu}_3(\text{Ta}_{1-x}\text{Nb}_x)_7\text{O}_{19}$  ( $0 < x \leq 0.15$ ) solid solution compositions.

## Particle Morphology

Results of the SEM images, shown in Figure 4-6, of  $\text{Cu}_3(\text{Ta}_{1-x}\text{Nb}_x)_7\text{O}_{19}$  with 5% Nb, 10% Nb and 15% Nb show micron-sized crystallites with highly faceted and smooth surfaces, ranging in size between  $\sim 5$  to  $20\ \mu\text{m}$ . Thus, there seems to be no impact of the Nb(V) substitution on the particle morphology and sizes of the  $\text{Cu}_3(\text{Ta}_{1-x}\text{Nb}_x)_7\text{O}_{19}$  ( $x = 0$  to  $0.15$ ) products, likely as a result of the similar preparative conditions for each

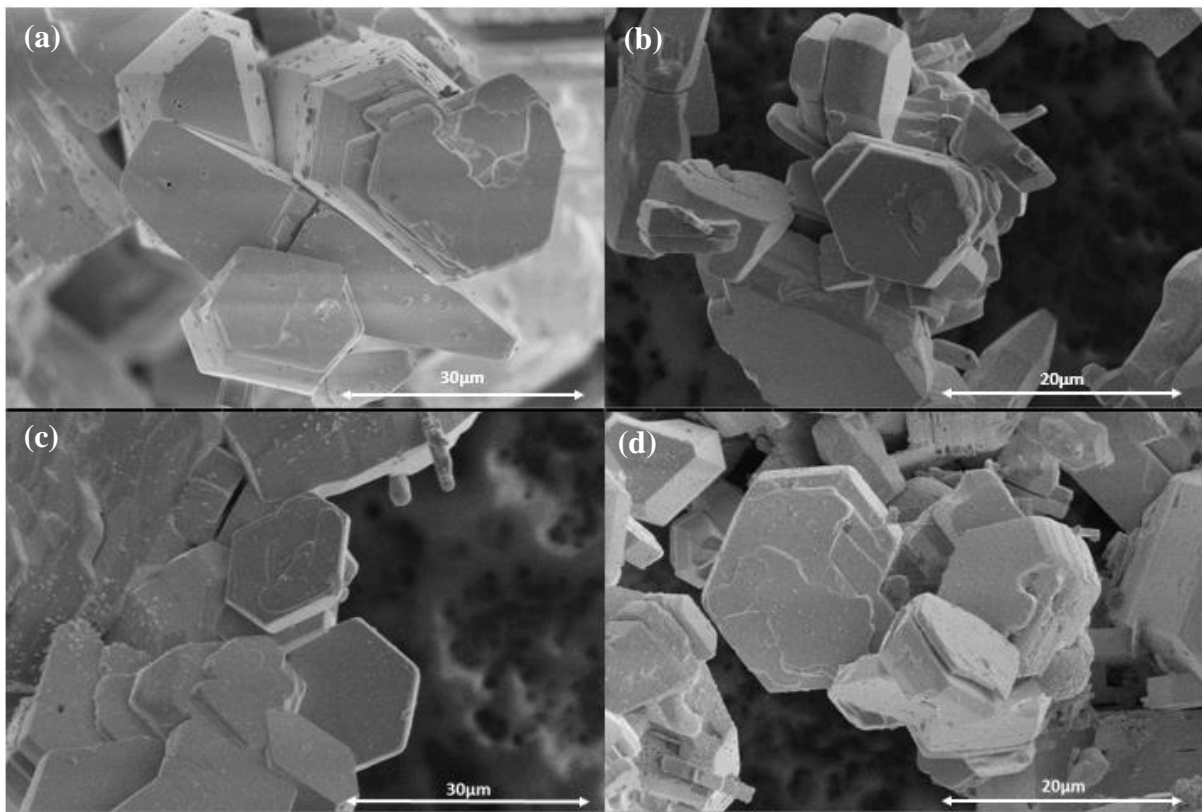


**Figure 4-6.** SEM images of  $\text{Cu}_3(\text{Ta}_{1-x}\text{Nb}_x)_7\text{O}_{19}$  solid solutions with 0% Nb (a), 5% Nb (b), 10% Nb (c) and 15% Nb (d) content.

## TGA analysis

Thermogravimetric analyses of members of the  $\text{Cu}_3(\text{Ta}_{1-x}\text{Nb}_x)_7\text{O}_{19}$  solid solution for 2% Nb, 5% Nb, 10% Nb, and 15% Nb have been carried out from 30 °C to 450 °C for 20mins, shown in Figure 4-7. Initially, the solid solution samples exhibited small weight losses owing to the removal of surface moisture. However, after all the surface water has been driven off, each sample gained weight owing to the oxidation of Cu(I) cations at the surfaces. Similar weight gains were observed for each member of the solid solution, and which was relatively small (~0.45%). Listed in Table 3-4 are the weight gains of each of the solid solutions. Further experiments are necessary in order to understand the chemical reactions which are responsible for the weight gains.

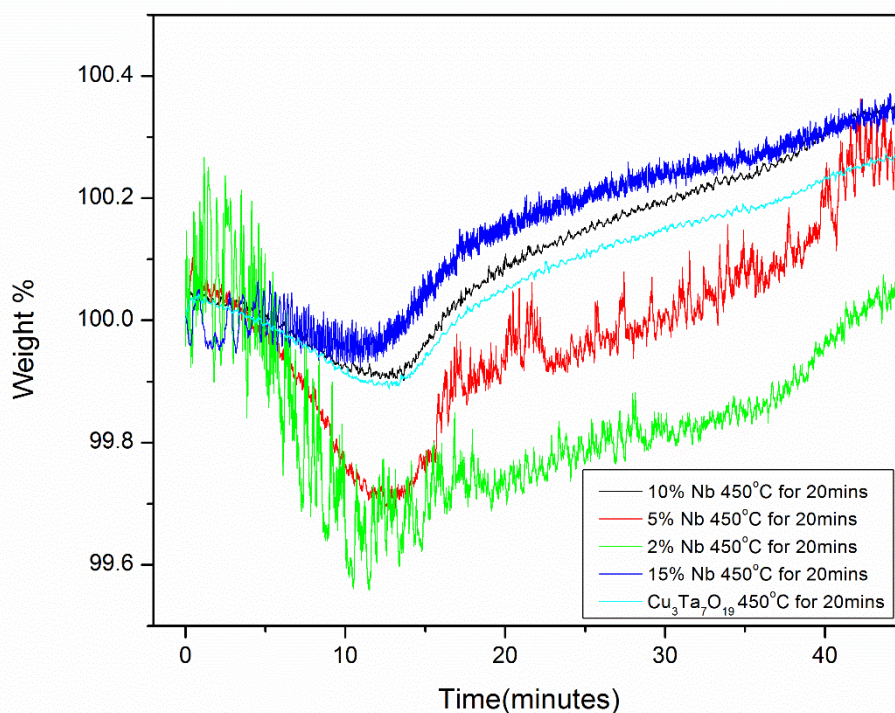


**Figure 4-7.** TGA analysis of  $\text{Cu}_3(\text{Ta}_{1-x}\text{Nb}_x)_7\text{O}_{19}$  films heated to 450 °C for 20mins, with ramping up and down time of 15 minutes and 10 minutes, respectively.

**Table 4-1.** Weight gains from thermogravimetric analyses for members of the  $\text{Cu}_3(\text{Ta}_{1-x}\text{Nb}_x)_7\text{O}_{19}$  solid solution heated to at 450 °C for 20 minutes.

Solid Solution	Increase in Weight (%)
0% Nb	0.3786
2% Nb	0.3986
5% Nb	0.5938
10% Nb	0.4390
15% Nb	0.3853

### Mott-Schottky Measurements

To investigate the impact of Nb(V) substitution on the band energies of  $\text{Cu}_3(\text{Ta}_{1-x}\text{Nb}_x)_7\text{O}_{19}$ , Mott-Schottky measurements were carried out for each of the solid solution members, as described in the Experimental Techniques section in Chapter 2.

In each case, the valence-band energies of each of the solid solution films changed only by a few hundredths of a volt. The valence band energy of each solid solution is primarily determined by the contributions from the Cu  $3d^{10}$  orbitals, which shows only small detectable changes with the substitution of Nb(V) for Ta(V) cations. However, as listed in Table 4-2, the conduction band shifts to lower energies by ~0.4V, consistent with the decrease in the bandgap sizes. Additional experiments are necessary to confirm these results.

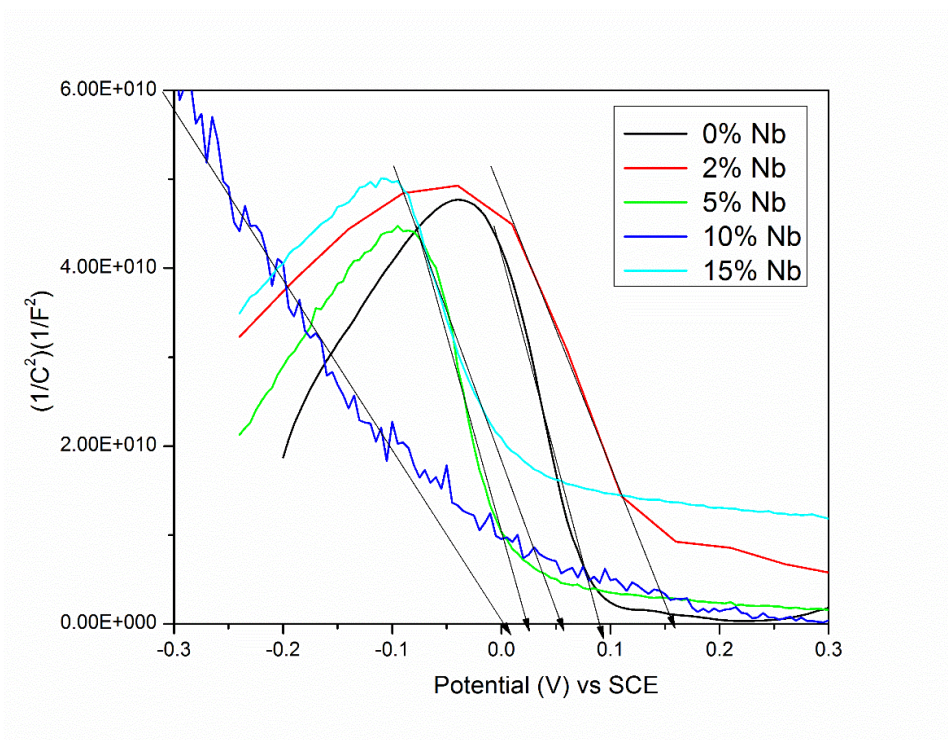


**Figure 4-8.** Results of Mott-Schottky measurements of members of the  $\text{Cu}_3(\text{Ta}_{1-x}\text{Nb}_x)_7\text{O}_{19}$  solid solution, with the applied potential from 0.3 to -0.3V at pH ~6.3.

**Table 4-2.** Measured flat-band potentials vs SHE and calculated redox potential of the valence-band edge for  $\text{Cu}_3(\text{Ta}_{1-x}\text{Nb}_x)_7\text{O}_{19}$  films (pH ~6.3)

Solid Solution	Flat-band Potential, V	Valence band energy, V	Conduction band energy, V	Band gap, eV
0% Nb	0.3556	0.727	-1.573	2.3
2% Nb	0.3156	0.629	-1.37	2.0
5% Nb	0.3656	0.7368	-1.16	1.9
10% Nb	0.2756	0.6468	-1.153	1.9
15% Nb	0.3006	0.6484	-1.151	1.8

## Photoelectrochemical Properties

Previous photoelectrochemical measurements on *p*-type  $\text{Cu}_3\text{Ta}_7\text{O}_{19}$  polycrystalline films showed significant photocurrents up to  $\sim -0.10 \text{ mA/cm}^2$  under visible-light irradiation and no heating in air. The current density increased with the oxidation temperature. Linear sweep voltammetry measurements on polycrystalline films of  $\text{Cu}_3(\text{Ta}_{1-x}\text{Nb}_x)_7\text{O}_{19}$  ( $0 < x \leq 0.15$ ) was performed under visible-light AM 1.5 G light within an applied bias of 0.2 V to -0.6 V, shown in Figures 4-9 to 4-13. Compared to pure  $\text{Cu}_3\text{Ta}_7\text{O}_{19}$ , the 2% Nb solid solution shows a larger cathodic photocurrent ( $\sim -0.2 \text{ mA/cm}^2$ ). Films with 5%, 10% and 15% Nb solid solutions exhibited even higher photocurrents. The maximum photocurrent of  $-0.55 \text{ mA/cm}^2$  was with films of 15% Nb. To have more detail idea about the stability of the non-oxidized polycrystalline films chronoamperometric measurements were carried out. Constant biases (-0.25V) were applied and current density of the polycrystalline films were observed during these measurements.

Chronoamperometric data in Figure 4-11 show increased photo decay for films with the solid solutions for a time period of 1,000 seconds. Calculated photo decays are 54% for 0% Nb, 64% for 2% Nb, 50% for 5 and 15% Nb and 62% for 10% Nb, respectively.

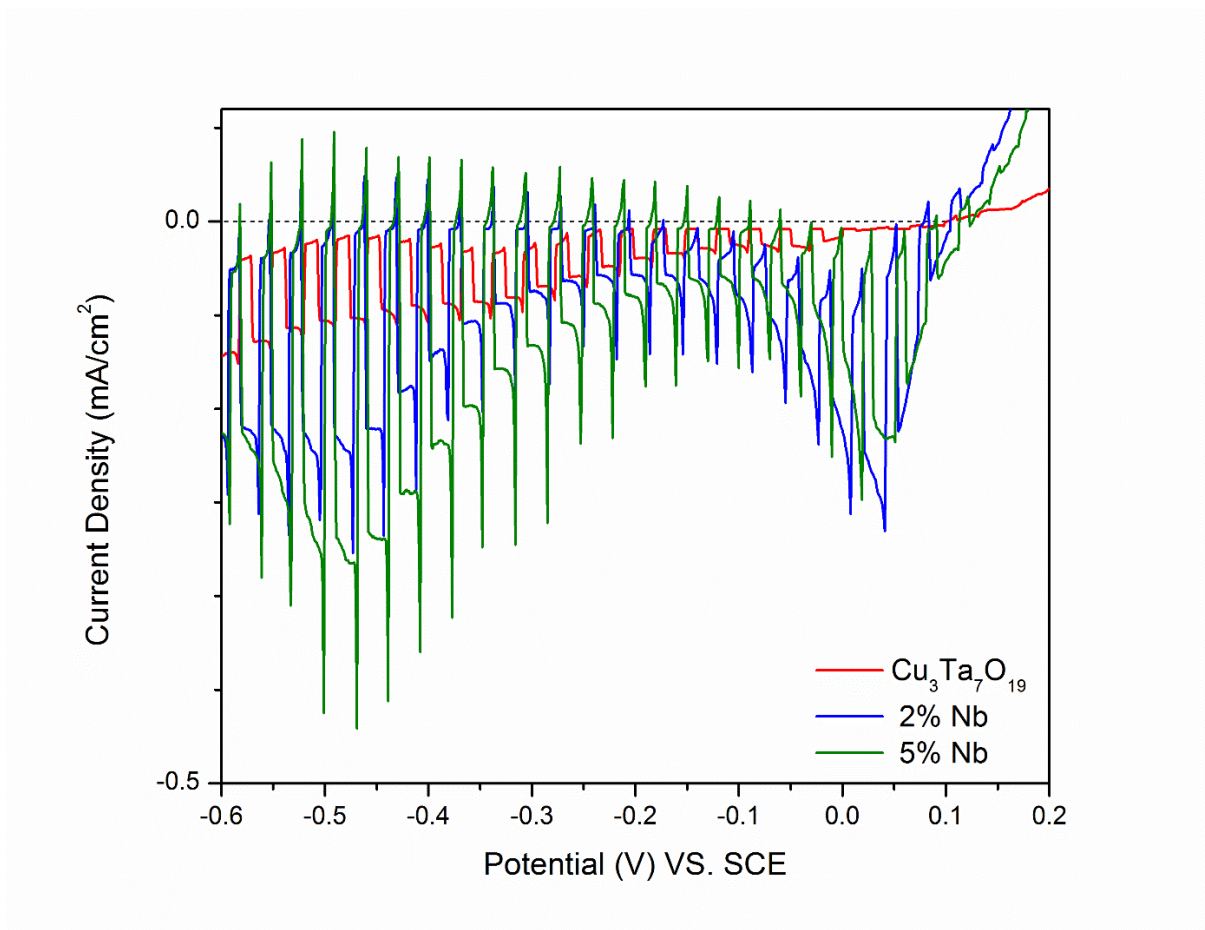


**Figure 4-9.** Current-potential curves in aqueous 0.5M Na<sub>2</sub>SO<sub>4</sub> solution at pH~6.3 under chopped visible light for Cu<sub>3</sub>(Ta<sub>1-x</sub>Nb<sub>x</sub>)<sub>7</sub>O<sub>19</sub> (x = 0, 0.02, 0.05) films annealed at 500 °C and no heating in air.

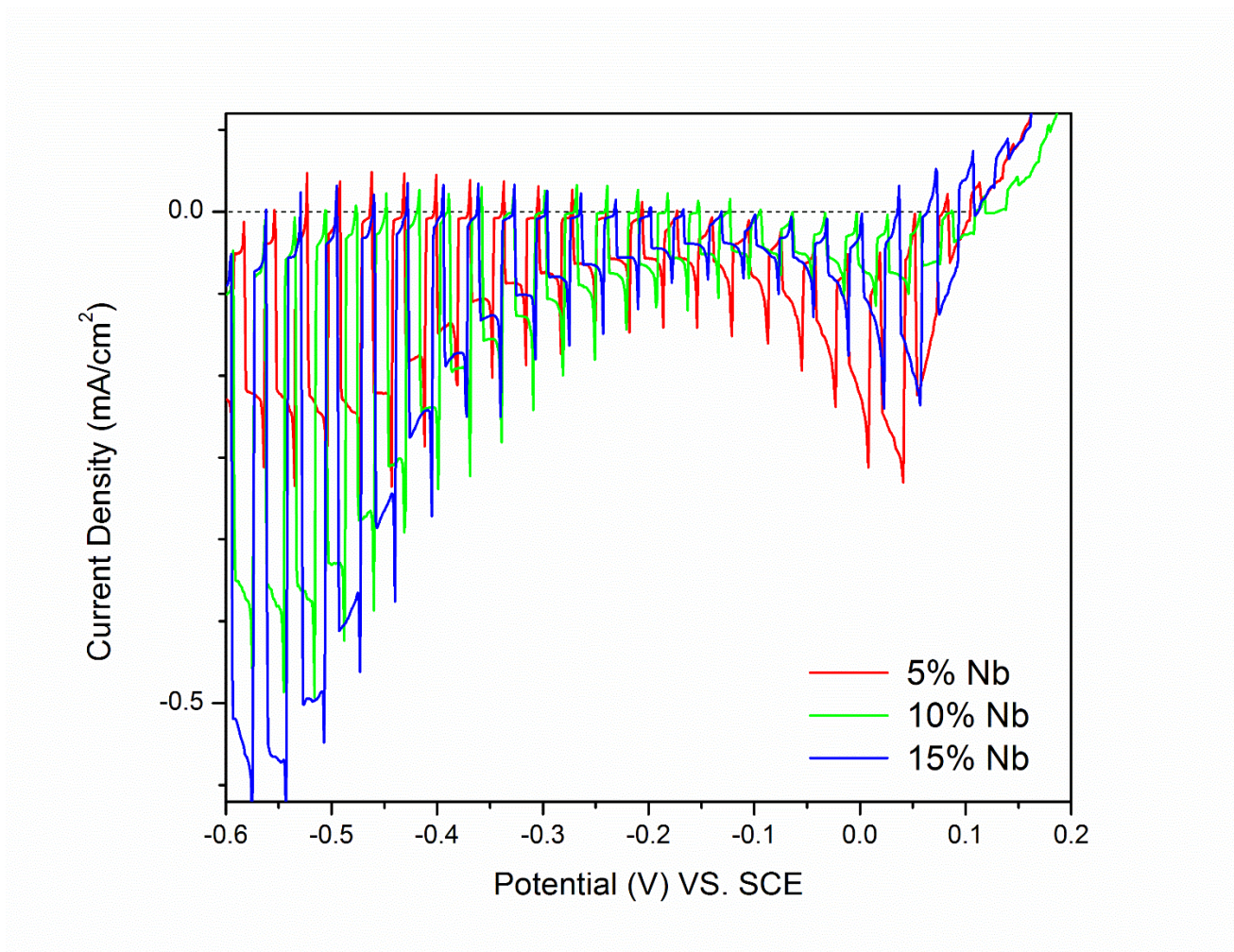


**Figure 4-10.** Current-potential curves in aqueous 0.5M Na<sub>2</sub>SO<sub>4</sub> solution at pH~6.3 under chopped visible light for Cu<sub>3</sub>(Ta<sub>1-x</sub>Nb<sub>x</sub>)<sub>7</sub>O<sub>19</sub> (x = 0.05, 0.1, 0.15) films annealed at 500 °C and no heating in air.

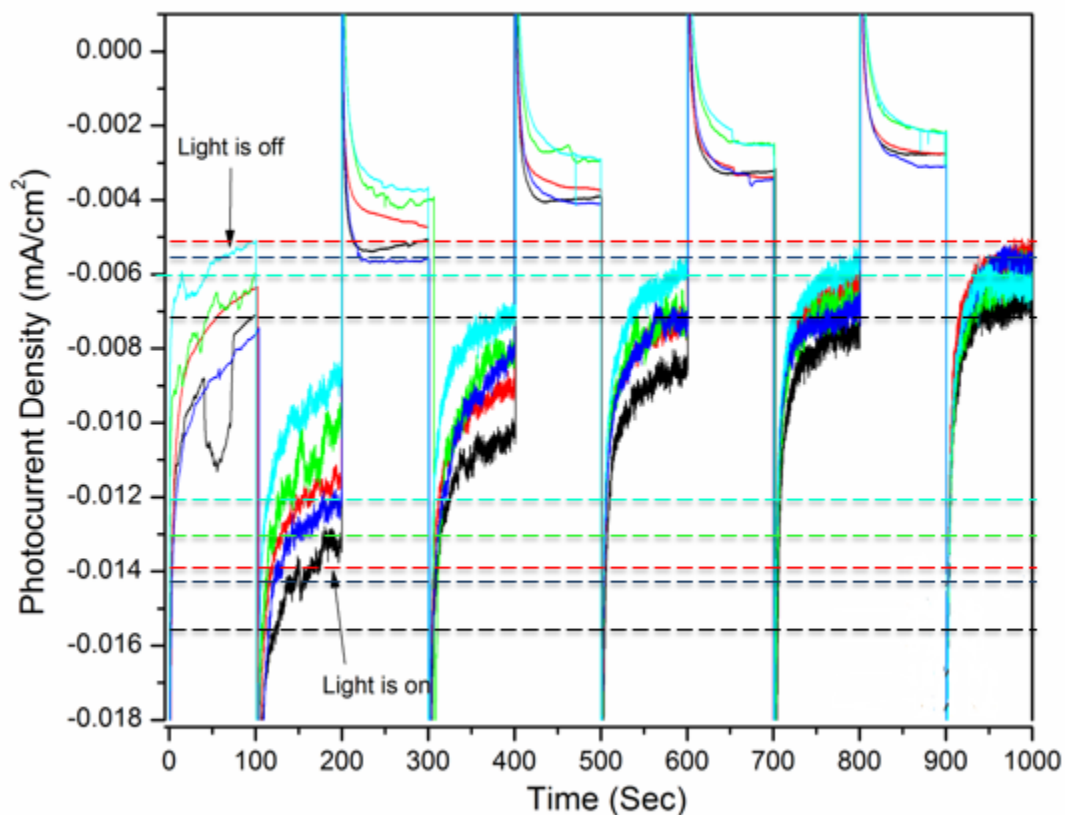


**Figure 4-11.** Chronoamperometry ( $-0.25\text{V}$  applied bias) in aqueous  $0.5\text{M Na}_2\text{SO}_4$  solution at  $\text{pH}\sim 6.3$  under chopped visible light for  $\text{Cu}_3(\text{Ta}_{1-x}\text{Nb}_x)_7\text{O}_{19}$  films annealed at  $500\text{ }^\circ\text{C}$  and no heating in air for 0% Nb (black), 2% Nb (red), 5% Nb (green), 10% Nb (blue), 15% Nb (cyan).

Solid solution polycrystalline films of  $\text{Cu}_3(\text{Ta}_{1-x}\text{Nb}_x)_7\text{O}_{19}$  ( $x = 0.02, 0.05, 0.1, 0.15$ ) were heated in air at  $250\text{ }^\circ\text{C}$ ,  $350\text{ }^\circ\text{C}$  and  $450\text{ }^\circ\text{C}$  for 20 minutes. Heating of the films turned them into darker color. Photoelectrochemical properties of the solid solution films were measured under the same condition as mentioned previously, shown in Figures 4-12 and 4-13. Except for the solid solution with 10% Nb, all the films with 2 to 15 percent of Nb shows similar trends in their photocurrents. Each film gave sizable photocurrents of about  $-0.7$  to  $-0.9$

mA/cm<sup>2</sup>, but which decreased for the films heated to 250 °C for 20 minutes. The largest photocurrent was observed for the films heated to 450 °C for 20 minutes and for the 10% Nb oxidation at 350 °C, at ~ -1.0 mA/cm<sup>2</sup>. As previously reported heating of the films creates surface-rich CuO regions as a result of Cu-extrusion from these types of structures. However, further experiments and analyses are necessary in order to understand the origins of these effects for Cu<sub>3</sub>(Ta<sub>1-x</sub>Nb<sub>x</sub>)<sub>7</sub>O<sub>19</sub>.

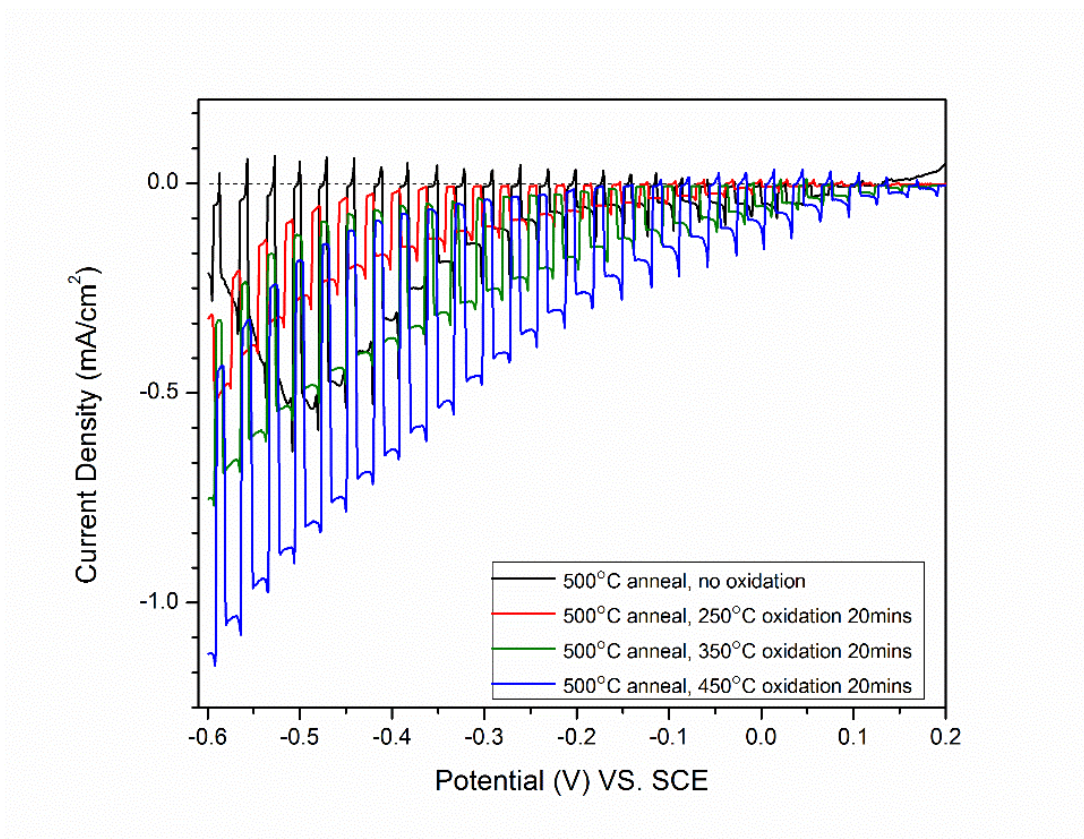


**Figure 4-12.** Current-potential curve in aqueous 0.5M Na<sub>2</sub>SO<sub>4</sub> solution at pH~6.3 under chopped visible light for Cu<sub>3</sub>(Ta<sub>1-x</sub>Nb<sub>x</sub>)<sub>7</sub>O<sub>19</sub> (x = 0.02) films annealed at 500 °C and not heated in air (black), or heated in air at 250 °C (red), 350 °C (green), or 450 °C (blue) for 20 minutes.

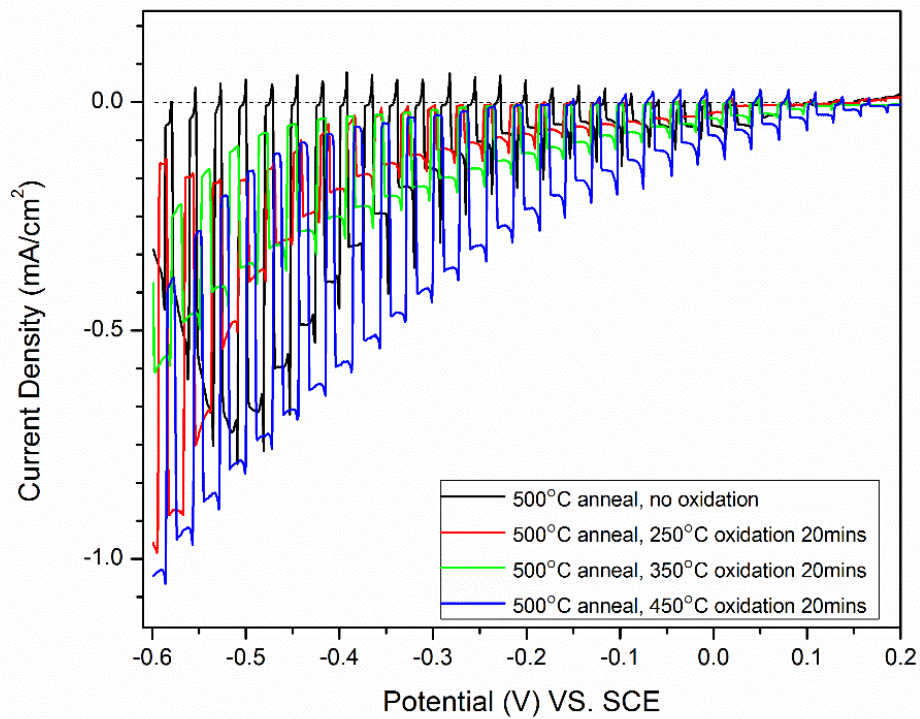


**Figure 4-13.** Current-potential curve in aqueous 0.5M Na<sub>2</sub>SO<sub>4</sub> solution at pH~6.3 under chopped visible light for Cu<sub>3</sub>(Ta<sub>1-x</sub>Nb<sub>x</sub>)<sub>7</sub>O<sub>19</sub> (x = 0.05) films annealed at 500 °C and not heated in air (black), or heated in air at 250 °C (red), 350 °C (green), or 450 °C (blue) for 20 minutes.

## Conclusion

Members of the  $\text{Cu}_3(\text{Ta}_{1-x}\text{Nb}_x)_7\text{O}_{19}$  ( $x = 0$  to  $0.15$ ) solid solution have been prepared in high purity by molten-flux synthesis methods. Results of UV-Vis diffuse reflectance spectroscopy measurements show a significant amount of red shift in both direct and indirect band gap transition with increasing Nb(V) substitution. The polycrystalline films of the solid solutions show comparable photocurrents with the parent  $\text{Cu}_3\text{Ta}_7\text{O}_{19}$  phase, with an increase in the photocurrent density with 0 to 15% Nb content. The films heated to  $450^\circ\text{C}$  yields the highest photocurrent densities. Results of Mott-Schottky measurements show that there is almost no change in valence-band energy, but a significant lowering of the conduction band energy as a result of the lower-energy Nb d-orbitals.

## CHAPTER 5

### SOLID STATE SYNTHESIS AND CHARACTERIZATION OF $\text{Cu}_2\text{Mo}_{2.4}\text{V}_{1.6}\text{O}_{12}$

#### Introduction

The Cu(I)-molybdate system consists of several compounds, e.g.,  $\text{Cu}_4\text{Mo}_5\text{O}_{17}$ ,  $\text{Cu}_6\text{Mo}_5\text{O}_{18}$  and  $\text{Cu}_4\text{Mo}_6\text{O}_{20}$ ,<sup>54-56</sup> all of which have very small band gap sizes and low conduction band energies that are not suitable for photocatalytic hydrogen production. On the other hand, Cu(I)-vanadates such as  $\text{Cu}_3\text{VO}_4$ , which has a larger band gap size of  $\sim 1.23$  eV,<sup>51</sup> have higher conduction band energies at sufficiently negative potentials for photocatalytic hydrogen production. Thus, it was hypothesized that the substitution of vanadium into Cu(I)-molybdate phases could be used to shift their bandgap sizes and conduction bands to more favorable energies, i.e., to more negative reduction potentials.<sup>50,51</sup> There have been no prior reported compounds in the Cu(I)-molybdate/vanadate system.

Initial reactions were investigated in order to substitute vanadium for molybdenum within the known  $\text{Cu}_4\text{Mo}_6\text{O}_{20}$  phase. During these synthetic efforts a new Cu(I)-molybdate/vanadate compound was discovered. The new compound, determined to have the chemical formula  $\text{Cu}_2\text{Mo}_{2.4}\text{V}_{1.6}\text{O}_{12}$ , was structurally characterized from single crystal X-ray diffraction refinements, and further characterized using a combination of UV-Vis diffuse reflectance spectroscopy, scanning electron microscopy and energy-dispersive X-ray spectroscopy (EDS). Thus, described herein is the crystalline structure and properties of the first known Cu(I)-molybdate/vanadate phase.

## Experimental

### Synthesis

Solid state reaction methods were used in the preparation of  $\text{Cu}_2\text{Mo}_{2.4}\text{V}_{1.6}\text{O}_{12}$ .  $\text{Cu}_2\text{O}$  (Alfa Aesar, 99.99%),  $\text{MoO}_3$  (Alfa Aesar, 99.99%) and  $\text{V}_2\text{O}_5$  (Alfa Aesar, 99.99%) were well ground using a mortar and pestle in a 2:3.5:1.5 molar ratio. This reactant mixture was next loaded into a fused-silica tube and flame sealed under vacuum. The reaction vessel was heated at 900 °C for 96 hours, with heating and cooling times of 4 hours. The resulting product contained dark, shiny, and lustrous single crystals.

### Characterization

#### X-ray Diffraction Techniques

A single-crystal X-ray data set was collected on a Bruker-APEX-II CCD diffractometer using graphite-monochromatized Mo  $K\alpha$  radiation ( $\lambda = 0.71073 \text{ \AA}$ ) from a sealed tube at 296 K. The unit cell obtained formed in the monoclinic crystal system with cell parameters of  $a = 9.4830(3) \text{ \AA}$ ,  $b = 3.69480(10) \text{ \AA}$ ,  $c = 6.4696(2) \text{ \AA}$ ,  $\beta = 111.4620(11)^\circ$ . The reflection intensities were integrated with the SAINT subprogram in the SMART software package. A space group determination was made ( $C2$  No. 5) and the structure was solved and refined using the WinGX and SHELXL-97 software packages and associated subprograms. The structure was refined by full matrix least squares on  $F^2$  with anisotropic thermal parameters, and converged to  $R_1/wR_2 = 0.0216/0.538$  and a goodness-of-fit = 1.075. Selected single crystal diffraction data and refined atomic parameters for  $\text{Cu}_2\text{Mo}_{2.4}\text{V}_{1.6}\text{O}_{12}$  are listed in Tables 5-1 and 5-2.

#### Optical Properties

In order to characterize the bandgap energy of  $\text{Cu}_2\text{Mo}_{2.4}\text{V}_{1.6}\text{O}_{12}$ , UV-visible diffuse reflectance spectroscopy was used. The experimental methods for this technique have been described in Chapter 2. The chemical composition, and particles sizes and morphologies, were characterized by scanning electron microscopy (SEM) using a JEOL JSM-6400F field-

emission scanning electron microscope. An acceleration voltage of 10.0 kV was used, and images were collected by an Everhart-Thornley secondary electron detector.

## Results and Discussions

### Crystal Structure

As listed in Table 5-2, the  $\text{Cu}_2\text{Mo}_{2.4}\text{V}_{1.6}\text{O}_{12}$  crystal structure consists of one symmetry unique copper site, one site-disordered molybdenum/vanadium site, one vanadium site, and three oxygen sites. The crystal structure consists of one-dimensional  $\text{CuO}_6$  octahedral chains and  $\text{MoO}_6/\text{VO}_6$  octahedral layers, shown in Figure 5-1. Within the  $\text{CuO}_6$  distorted octahedra, two different elongated bonds are formed between  $\text{Cu}(2) - \text{O}(4)$  and  $\text{Cu}(2) - \text{O}(4)$  with interatomic distances of  $2.419(2) \text{ \AA}$  and  $2.362(2) \text{ \AA}$ , respectively. Other two shorter bonds of  $\text{Cu}(2) - \text{O}(3)$  are found to be at  $1.938(2) \text{ \AA}$ . The  $\text{O}(3)$  and  $\text{O}(4)$  atoms connect  $\text{MoO}_6/\text{VO}_6$  layers to the  $\text{CuO}_6$  chains. As shown in Figure 5-2(b), the  $\text{MoO}_6/\text{VO}_6$  octahedra form layers from edge- and corner-sharing oxygen atoms.

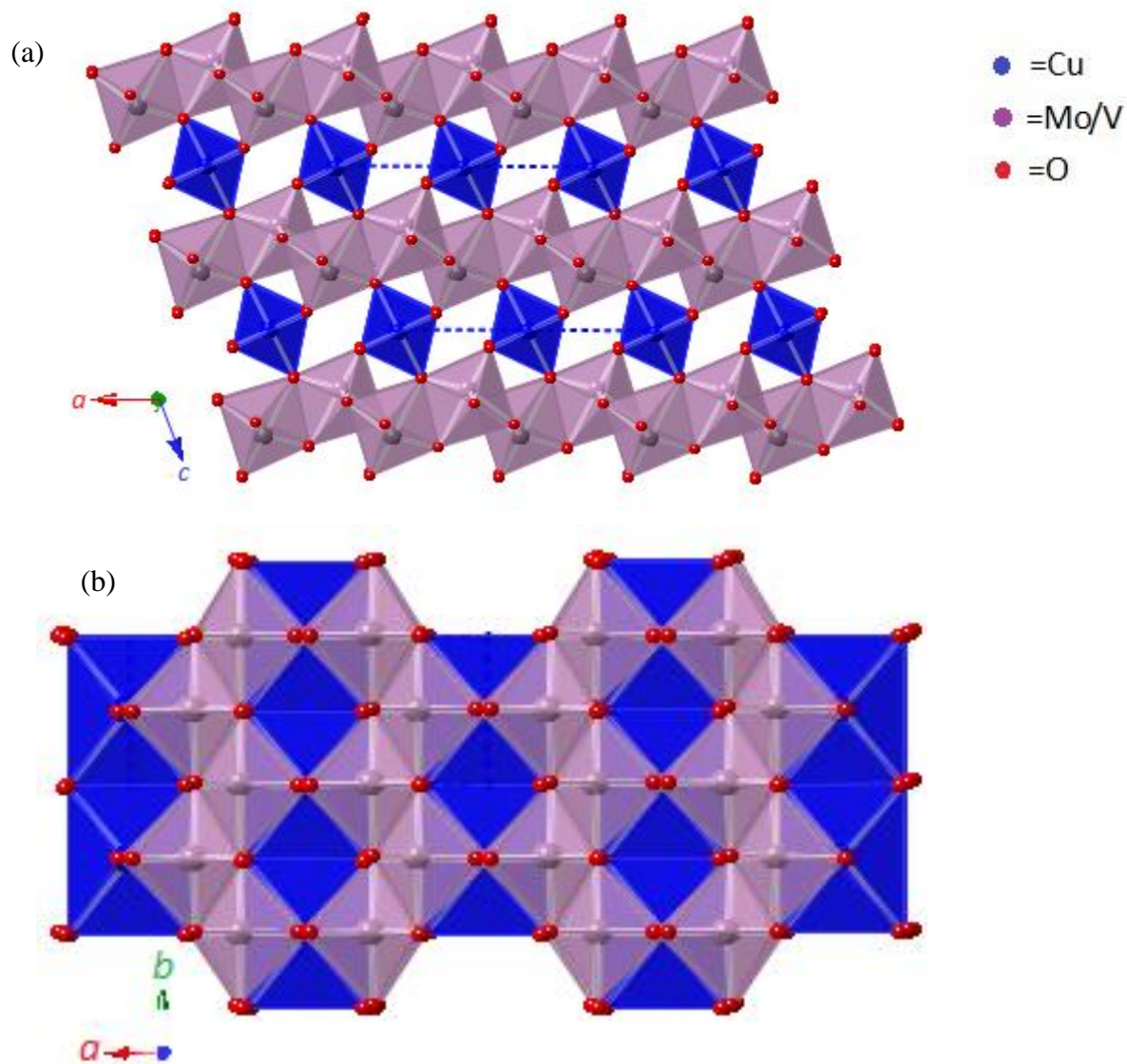


**Figure 5-1.** Polyhedral views with the projections along *b*-axis (a) and *c*-axis (b) of the unit cell of  $\text{Cu}_2\text{Mo}_{2.4}\text{V}_{1.6}\text{O}_{12}$ .

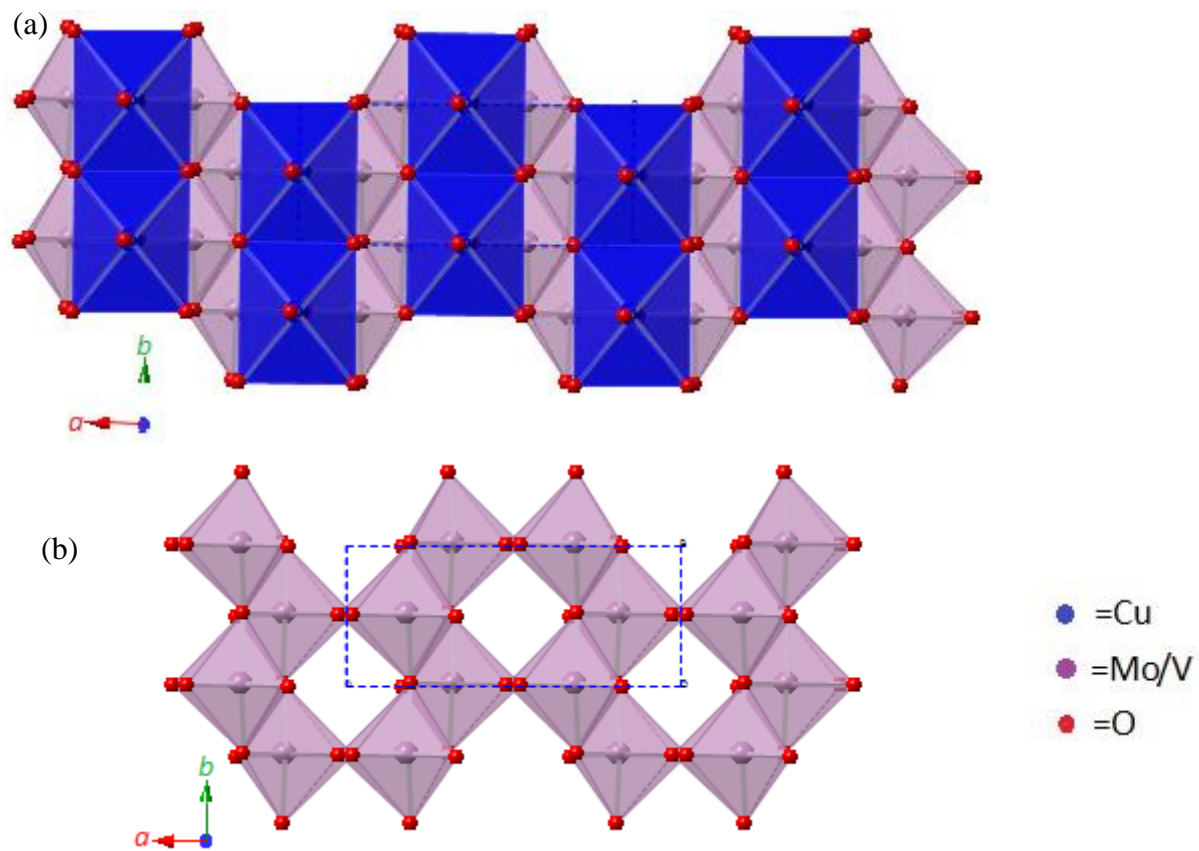


**Figure 5-2.** Polyhedral views with the (a) Cu-layers along  $c$ -axis of  $\text{Cu}_2\text{Mo}_{2.4}\text{V}_{1.6}\text{O}_{12}$  and (b) Mo-layer along the  $c$ -axis

**Table 5-1.** Selected single crystal data for  $\text{Cu}_2\text{Mo}_{2.4}\text{V}_{1.6}\text{O}_{12}$ 

<b>Formula</b>	<b><math>\text{Cu}_2\text{Mo}_{2.4}\text{V}_{1.6}\text{O}_{12}</math></b>
Formula Weight	804.72
Space group	$C2$ (No.5)
Radiation	Mo $K\alpha$ $\lambda = 0.71073 \text{ \AA}$
Crystal system	Monoclinic
Temperature, K	299(2)
$a/\text{\AA}$	9.4830(3)
$b/\text{\AA}$	3.69480(10)
$c/\text{\AA}$	6.4696(2)
$\beta^\circ$	111.4620(11)
Volume/ $\text{\AA}^3$	210.962(11)
$Z$	1
$2\theta$ (°) range	3.384 – 35.161
$\mu$ ( $\text{mm}^{-1}$ )	12.870
Total reflections, $R_{\text{int}}$	2642, 0.0172
$R_1/R_w$	0.0216/0.0538
GOF	1.075

**Table 5-2.** Atomic coordinates and equivalent isotropic displacement parameters ( $\text{\AA}^2$ ).

Atomic positions	<i>X</i>	<i>y</i>	<i>z</i>	$U_{eq}$ ( $\text{\AA}^2$ )
Mo (1)	0.31709(3)	0.02262(2)	0.35315(5)	0.01579(11)
V (1)	0.31709(3)	0.02262(2)	0.35315(5)	0.01579(11)
Cu(2)	0.0000	-0.486(2)	0.0000	0.0590(5)
O (3)	0.4792(3)	0.012(3)	0.2870(4)	0.0198(5)
O (4)	0.1715(3)	0.004(4)	0.1075(5)	0.0219(9)
O (5)	0.3090(2)	0.524(3)	0.4356(4)	0.0166(4)

**Table 5-3.** Selected interatomic distances ( $\text{\AA}$ ) in the  $\text{Cu}_2\text{Mo}_{2.4}\text{V}_{1.6}\text{O}_{12}$  structure.

Bond Length Type	Distance( $\text{\AA}$ )
Mo(1) - O(4)	1.683(3)
-O(3)	1.741(2)
-O(5)	1.926(11)
-O(5)	1.938(11)
-O(5)	2.1201(18)
-O(3)	2.421(3)
Cu(2) - O(3)	1.938(3)
-O(3)	1.938(3)
-O(4)	2.363(14)
-O(4)	2.363(14)
-O(4)	2.418(15)
-O(4)	2.418(15)
V(1) -O(3)	2.421(3)
-O(5)	1.926(11)
-O(5)	2.1201(18)

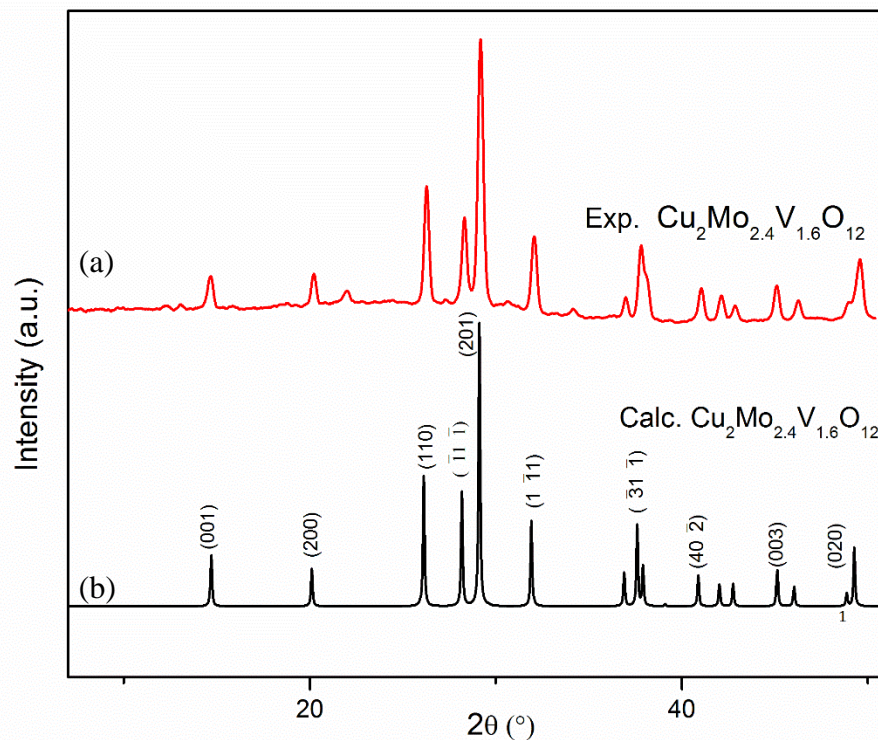


**Figure 5-3.** The indexed powder X-ray diffraction data for  $\text{Cu}_2\text{Mo}_{2.4}\text{V}_{1.6}\text{O}_{12}$  with the experimental (a) and calculated (b) patterns shown. The Miller indices ( $h$ ,  $k$ ,  $l$ ) are shown on the calculated pattern.

### Energy-dispersive X-ray spectroscopy

The chemical composition of the compound was further characterized and confirmed using energy-dispersive X-ray spectroscopy (EDS) for elemental analysis. The EDS data show the presence of both vanadium and molybdenum within the crystallites, consistent with the final refined chemical formula of the single crystal. Figure 5-4 shows the SEM images and the EDS data of the  $\text{Cu}_2\text{Mo}_{2.4}\text{V}_{1.6}\text{O}_{12}$  particles.

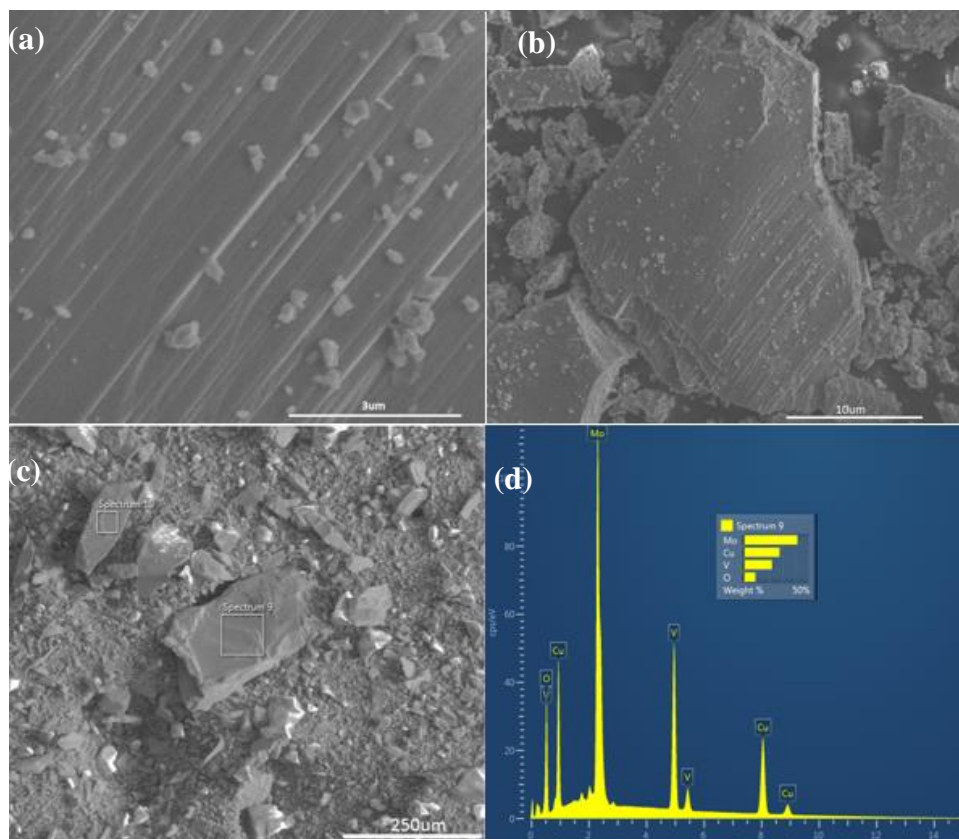


**Figure 5-4.** Scanning-electron microscopy images of the surfaces of a  $\text{Cu}_2\text{Mo}_{2.4}\text{V}_{1.6}\text{O}_{12}$  particle (a and b) and energy dispersive X-ray spectroscopy of a  $\text{Cu}_2\text{Mo}_{2.4}\text{V}_{1.6}\text{O}_{12}$  particle (c and d).

### Optical Properties

Within this new Cu(I)-molybdate/vanadate compound, both V  $3d^0$  and Mo  $4d^0$  orbitals are present together with the Cu(I)  $3d^{10}$  orbitals, suggesting a bandgap size should result that is intermediate between the Cu(I)-vanadates and Cu(I)-molybdates. As shown in Figure 5.5, direct and indirect bandgap transitions of  $\sim 1.7$  eV and  $\sim 1.4$  eV were determined. These results are close to that found for both Cu(I)-molybdates as well as Cu(I)-vanadates. Further investigations are necessary to understand the origins of the electronic bandgap transitions in this new compound.

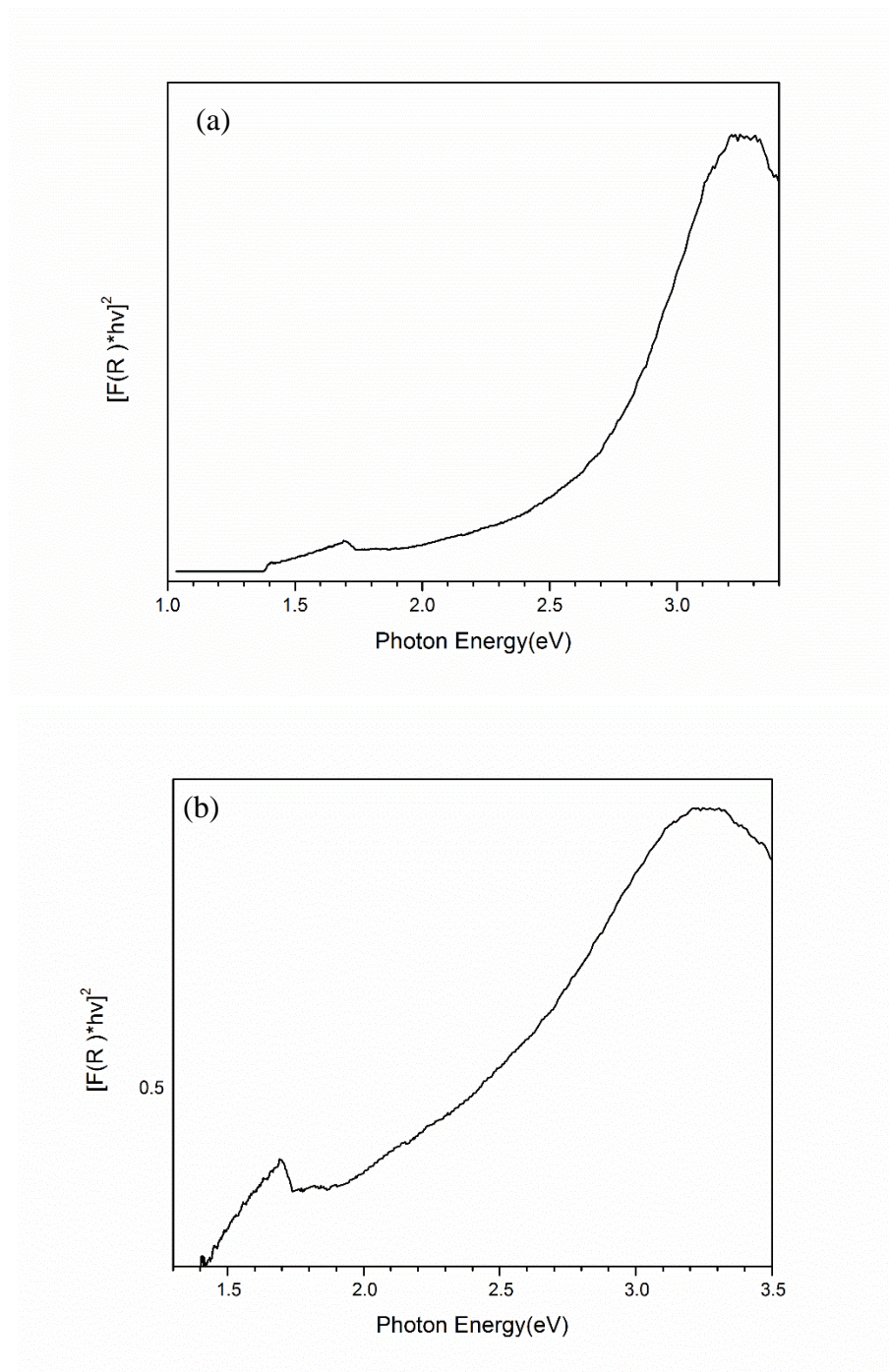


**Figure 5-5.** Tauc Plots of direct (a) and indirect (b) transitions in  $\text{Cu}_2\text{Mo}_{2.4}\text{V}_{1.6}\text{O}_{12}$ .

## Conclusions

The first known Cu(I)-molybdate/vanadate phase, i.e.,  $\text{Cu}_2\text{Mo}_{2.4}\text{V}_{1.6}\text{O}_{12}$ , has been synthesized using solid state methods and its structure has been characterized using single X-ray diffraction. The compound contains chains of  $\text{Cu(I)O}_6$  octahedra and layers of  $\text{V(V)O}_6/\text{Nb(V)O}_6$  octahedra that bridge via shared edges and vertices. UV-Vis diffuse reflectances of the powder shows relatively low-energy direct and indirect bandgap transitions of  $\sim 1.7\text{eV}$  and  $\sim 1.4\text{eV}$ , respectively. Future work will be necessary to understand the structure and properties of this new compounds, such as including X-ray photoelectron spectroscopy, its range of chemical composition, electronic structure calculations, and measurements of its photocatalytic and photoelectrochemical properties.

**PART 3**  
**CONCLUSIONS**

Semiconducting metal oxides are the most promising photocatalysts for photoelectrochemical production of hydrogen by the splitting of water using solar light.<sup>59,60</sup> Discovery of new semiconducting oxides has drawn intense attention for last few years. A critical focus of this field of research is to develop materials with appropriate band energies and bandgap sizes in order to work under visible-light and also straddle the  $H^+/H_2$  and  $O_2/H_2O$  redox potentials. Previous studies by the Maggard group indicate that mixed metal oxides with a combination of early ( $d^0$ ) and late transitional metals ( $d^{10}$ ) can be used as a visible-light photocatalyst due to their lower band gap sizes.<sup>35,46,51</sup> The optical and photoelectrochemical properties of Cu(I) containing semiconducting  $Cu_3Ta_7O_{19}$  and its solid solution with varying percentages of Nb(V), as well as a new copper-molybdate/vanadate compound, i.e.,  $Cu_2Mo_{2.4}V_{1.6}O_{12}$ , have been presented. Previously,  $Cu_3Ta_7O_{19}$  has been synthesized by flux methods, and heating of the material in air gives higher photocurrent owing to the formation of Cu(II)-rich surface regions, but the relationship between the heating time and temperature with the photocurrent was not well known.<sup>61</sup> These investigations have shown that a regular trend is observed for the production of higher cathodic photocurrents. Polycrystalline films were investigated by powder XRD, but no impurities were detected and a clear shift in the peak position to lower  $2\theta$  ( $^\circ$ ) was observed. Lattice refinement indicates an increase of the unit cell volume of the material. As previously reported for the other similar phases, heating of the material causes oxidation of Cu(I) cation to CuO and migration of Cu(I) cation to the surface, and increasing the photocurrent.<sup>36,58</sup> In the second part of the research, the  $Cu_3(Ta_{1-x}Nb_x)_7O_{19}$  solid solution was synthesized in order to characterize the impact of Nb(V) substitution on the bandgap size and band energies. Up to 15% Nb(V) cations could be substituted for the Ta(V) cations, with the bandgap size exhibiting a red shift from  $\sim 2.3$  eV to  $\sim 1.9$  eV. From the Mott-Schottky calculations it has been shown that the valence band position stays relatively constant, while the conduction band is lowered in energy, i.e., to less negative potentials, owing to the lower energy Nb( $4d^0$ ) orbitals replacing the higher energy of Ta( $5d^0$ ) orbitals. Photoelectrochemical properties of polycrystalline films of the solid solutions shows increased photocurrents compared to the parent  $Cu_3Ta_7O_{19}$  phase. Further, there is a linear increase in photocurrent density with an increase of the Nb content in the solid solution. The third part of

the research investigated the synthesis and structural determination of a new Cu(I)-molybdate/vanadate phase. Single crystal structure refinement yielded a chemical formula of  $\text{Cu}_2\text{Mo}_{2.4}\text{V}_{1.6}\text{O}_{12}$ , consistent with that obtained from energy dispersive X-ray spectroscopy (EDS) data. Optical property measurements show an indirect bandgap size of  $\sim 1.4$  eV for the shiny black product.

## REFERENCES

- (1) Fracastoro, G. **2014**, *02003*, 1–10.
- (2) Goldemberg, J.; Siqueira Prado, L. T. *Energy Policy* **2013**, *54*, 62–65.
- (3) *Photoelectrochemical Hydrogen Production*; van de Krol, R., Grätzel, M., Eds.; Electronic Materials: Science & Technology; Springer US: Boston, MA, 2012; Vol. 102.
- (4) Nocera, D. G.; Nash, M. P. **2007**, *104* (42).
- (5) Honda, K. & Fujishima, A. Electrochemical photolysis of water at a semiconductor electrode. *Nature* **1972**, *238*, 37–38.
- (6) NREL 2009 AM 1.5 Global solar spectrum derived from SMARTS v.2.9.2 <http://rredc.nrel.gov/solar/spectra/am1.5/>.
- (7) Kudo, A.; Miseki, Y. *Chem. Soc. Rev.* **2009**, *38* (1), 253–278.
- (8) Graetz, J. *Chem. Soc. Rev.* **2009**, *38* (1), 73–82.
- (9) Krol, R. Van De; Gr, M. **2012**, *102*, 3–11.
- (10) Aroutiounian, V. M.; Arakelyan, V. M.; Shahnazaryan, G. E. *Sol. Energy* **2005**, *78* (5), 581–592.
- (11) Milek, M.; Heinemann, F. W.; Khusniyarov, M. M. **2013**.
- (12) Gyu, H.; Won, D.; Won, S.; Hyeon, J.; Sung, J. **2003**, *91* (December).
- (13) Kudo, A.; Kato, H.; Nakagawa, S. **2000**, *7*, 571–575.
- (14) Wang, Y.; Shi, R.; Lin, J.; Zhu, Y. *Energy Environ. Sci.* **2011**, *4* (8), 2922.
- (15) Behnajady, M. A; Modirshahla, N.; Hamzavi, R. *J. Hazard. Mater.* **2006**, *133* (1-3), 226–232.
- (18) Ng, Y. H.; Iwase, A.; Kudo, A.; Amal, R. *J. Phys. Chem. Lett.* **2010**, *1* (17), 2607–2612.
- (16) Hara, M.; Kondo, T.; Komoda, M.; Ikeda, S.; Shinohara, K.; Tanaka, A. **1998**, *2*, 357–358.

- (17) Grigorovici, R.; Vancu, A. **1966**, 627, 627–637.
- (18) Zhang, D. *Acta Chim. Slovaca* **2013**, 6 (1), 141–149.
- (19) Konta, R.; Ishii, T.; Kato, H.; Kudo, A. **2004**, 8992–8995.
- (20) Roon, V.; Leeuw, D.; Breakdown, S. W.; Zou, Z.; Ye, J.; Sayama, K.; Arakawa, H. **2002**, 704 (2000), 625–628.
- (21) Hill, J. C.; Choi, K. **2012**, No. 1.
- (22) Sivula, K.; Le Formal, F.; Grätzel, M. *ChemSusChem* **2011**, 4 (4), 432–449.
- (23) Kleiman-shwarsstein, A.; Hu, Y.; Forman, A. J.; Stucky, G. D.; Mcfarland, E. W. **2008**, No. 001, 15900–15907.
- (24) Liu, Z.; Zhao, Z.; Miyauchi, M. **2009**, 17132–17137.
- (25) Matsumoto, Y.; Hombo, J. **1994**, 2950–2951.
- (26) Memming, R. **1968**, 13 (August 1967), 1299–1310.
- (27) Jongh, P. E. De; Vanmaeckelbergh, D.; Kelly, J. J. **2000**, 147 (2), 486–489.
- (28) Brillet, J.; Yum, J.; Cornuz, M.; Hisatomi, T.; Solarska, R.; Augustynski, J.; Graetzel, M.; Sivula, K. **2012**, 6 (December), 2–6.
- (29) Bocarsly, A. B.; Bookbinder, D. C.; Dominey, R. N.; Lewis, N. S.; Wrighton, M. S. **1980**, 3683 (16).
- (30) Zou, Z.; Arakawa, H. *J. Photochem. Photobiol. A Chem.* **2003**, 158 (2-3), 145–162.
- (31) Chen, X.; Shen, S.; Guo, L.; Mao, S. S. **2010**, 6503–6570.
- (32) Bruker. *APEX2 Software Suite*. **2007**,
- (33) Joshi, U. A.; Maggard, P. A. **2012**.
- (34) Choi, J.; King, N.; Maggard, P. A. **2013**, No. 2, 1699–1708.
- (35) Joshi, U. A.; Palasyuk, A. M.; Maggard, P. A. **2011**, 13534–13539.

- (36) Sullivan, I.; Sahoo, P. P.; Fuoco, L.; Hewitt, A. S.; Stuart, S.; Dougherty, D.; Maggard, P. A. **2014**, No. I.
- (37) Fuoco, L.; Joshi, U. A.; Maggard, P. A. **2012**, 3–10.
- (38) Rodríguez-Carvajal, J.; Roisnel, T. *Mater. Sci. Forum* **2004**, 443-444, 123–126.
- (39) Gražulis, S.; Daškevič, A.; Merkys, A.; Chateigner, D.; Lutterotti, L.; Quirós, M.; Serebryanaya, N. R.; Moeck, P.; Downs, R. T.; Le Bail, A. *Nucleic Acids Res.* **2012**, 40 (Database issue), D420–D427.
- (42) Shakespeare, T.; Shakespeare, J. *Color Res. Appl.* **2003**, 28 (1), 4–14.
- (43) Palasyuk, O.; Palasyuk, A.; Maggard, P. A. *J. Solid State Chem.* **2010**, 183 (4), 814–822.
- (44) Bruker. *APEX2 Software Suite*. **2007**,
- (45) Sheldrick, G. *Acta Crystallographica Section A*. **2008**, 64, 112.
- (46) Sahoo, P. P.; Maggard, P. A. **2013**.
- (47) Albery, W. J.; O'Shea, G. J.; Smith, A. L. *J. Chem. Soc. Faraday Trans.* **1996**, 92, 4083
- (48) Maeda, K.; Takata, T.; Hara, M.; Saito, N.; Inoue, Y.; Kobayashi, H.; Domen, K. **2005**, 8286–8287.
- (49) Xing, C.; Zhang, Y.; Yan, W.; Guo, L. *Int. J. Hydrogen Energy* **2006**, 31 (14), 2018–2024.
- (50) Palasyuk, O.; Palasyuk, A.; Maggard, P. A. *Inorg. Chem.* **2010**, 49 (22), 10571–10578.
- (51) Sahoo, P. P.; Zoellner, B.; Maggard, P. A. *J. Mater. Chem. A* **2015**, 3 (8), 4501–4509.
- (52) King, N.; Sullivan, I.; Watkins-Curry, P.; Chan, J. Y.; Maggard, P. A. *J. Solid State Chem.* **2015**, 232, 1–9.
- (53) Deton, A. R.; Ashcroft, N. W. *Phys. Rev. A* **1991**, 43, 3161-3164
- (54) Kenntnis, Z.; Cu, K.; Muller-buschbaum, M. K. H. K.; Interesse, G.; Oxydation, D.; Cumoo, R.; Schlieljlich, I.; Cuo-moo, D. S.; Cumoo, C. D. V. **1985**, 530, 7–15.

- (55) O, S. K. V. C. U. M. O.; Muller-buschbaum, M. K. H. K. **1986**, *531*, 140–146.
- (56) Moini, A.; Peascoe, R.; Rudolf, P. R.; Clearfield, A. **1986**, 3782–3785.
- (57) NREL 2009 AM 1.5 Global solar spectrum derived from SMARTS v.2.9.2  
<http://rredc.nrel.gov/solar/spectra/am1.5/>.
- (58) Nacole King, Prangya Sahoo, Lindsay Fuoco, Sean Stuart, Daniel Dougherty, Yi Liu, Paul A. Maggard, "Cu-deficiency in the p-type semiconductor Cu(1-x)Nb<sub>3</sub>O<sub>8</sub>" *Chem. Mater.* **2014**, 26(6), 2095-2104 .
- (59) Linsebigler, A. L., Lu, G., Yates, J. T. *Chemical Reviews.* **1995**, 95, 735.
- (60) Maeda, K., Saito, N., Lu, D., INoue, Y ., Domen, K. *The Journal of Physical Chemistry C* . **2007**, 111, 4749
- (61) Fuoco, L. Flux Synthesis of Metal Oxides and Investigations of their Photoelectrochemical and Magnetic Properties, North Carolina State University, **2012**, Vol. 6, pp. 1–172.
- (61) Zhang, X.; Song, J.; Jiao, J.; Mei, X. *Solid State Sciences* **2010**, 12, 1215–1219.
- (62) Palasyuk, O.; Maggard, P. A. *J. Solid State Chem.* **2012**, 191, 263–270.
- (63) Gelderman, K.; Lee, L.; Donne, S. W. J. *Chem. Educ.* **2007**, 84, 685